Hydrogeomorphology of asymmetric meandering channels: experiments and field evidence

Jorge Darwin Abad[1], Davide Motta[2], Leo Guerrero[3], Marco Paredes[4], Julio M Kuroiwa[5], and Marcelo H García[6]

[1]Research, Education and Development, RED YAKU
[2]Northumbria University
[3]Louisiana State University
[4]SENAMHI
[5]Universidad Nacional de Ingenieria
[6]University of Illinois at Urbana Champaign

January 20, 2023

Abstract

Meandering channels display complex planform configurations with upstream- and downstream- skewed bends. Bend orientation is linked to near-field hydrodynamics, bed morphodynamic regime, bank characteristics, riparian vegetation, and geological environment, which are the modulating factors that act specially in high-amplitude and high-sinuosity conditions. Based on the interaction between hydrodynamics and morphodynamics, previous studies have suggested that sub- ($\beta < \beta R$) and super-resonant ($\beta > \beta R$) morphodynamic regimes (where β is the half width-to-depth ratio of the channel, and βR is the resonance condition) may trigger a particular bend orientation (upstream- and downstream-skewed, respectively). However, natural rivers exhibit both US-skewed and DS-skewed bend patterns along the same reach, independently of the morphodynamic regime. Little is known about the hydrogeomorphology (forced and free morphodynamic patterns) under these bend orientations. Herein, using the asymmetric Kinoshita laboratory channel, experiments under sub- and super-resonant conditions (with presence or absence of free bars) for upstream-and downstream-skewed conditions are performed. Additional, detailed field measurements at US-skewed and DS-skewed bends of different skewness along the Tigre River in Peru are presented. Conditions at field scale at high-sinuosity and high-amplitude bends filter out the influence of the morphodynamic regime, where nonlinear processes (e.g. width variation) directly the development of the three-dimensional flow structure, then to the erosional and depositional patterns, and then to the lateral migration patterns.

Hydrogeomorphology of asymmetric meandering channels: experiments and field evidence

J. D. Abad[1,2], D. Motta[3], L. Guerrero[4,5], M. Paredes[6], J. M.Kuroiwa[1], and M.H.Garcia[7]

[1]Universidad Nacional de Ingenieria, Lima, Peru
[2]RED YAKU, Lima, Peru
[3]Northumbria University, Newcastle upon Tyne, UK
[4]Lousiana State University, USA
[5]Universidad de Ingenieria y Tecnologia, Lima, Peru
[6]National Service of Meteorology and Hydrology-SENAMHI, Loreto, Peru
[7]University of Illinois at Urbana-Champaign, Illinois, USA

Key Points:

- Meandering channels develop upstream- and downstream-skewed bends
- Bed morphology in rivers is composed by steady and non-steady bedforms
- Downstream-skewed bends develop more developed bed morphology

Corresponding author: Jorge D. Abad, `jabad@redyaku.com`

Abstract

Meandering channels display complex planform configurations with upstream- and downstream-skewed bends. Bend orientation is linked to near-field hydrodynamics, bed morphodynamic regime, bank characteristics, riparian vegetation, and geological environment, which are the modulating factors that act specially in high-amplitude and high-sinuosity conditions. Based on the interaction between hydrodynamics and morphodynamics, previous studies have suggested that sub- ($\beta < \beta_R$) and super-resonant ($\beta > \beta_R$) morphodynamic regimes (where β is the half width-to-depth ratio of the channel, and β_R is the resonance condition) may trigger a particular bend orientation (upstream- and downstream-skewed, respectively). However, natural rivers exhibit both US-skewed and DS-skewed bend patterns along the same reach, independently of the morphodynamic regime. Little is known about the hydrogeomorphology (forced and free morphodynamic patterns) under these bend orientations. Herein, using the asymmetric Kinoshita laboratory channel, experiments under sub- and super-resonant conditions (with presence or absence of free bars) for upstream-and downstream-skewed conditions are performed. Additional, detailed field measurements at US-skewed and DS-skewed bends of different skewness along the Tigre River in Peru are presented. Conditions at field scale at high-sinuosity and high-amplitude bends filter out the influence of the morphodynamic regime, where nonlinear processes (e.g. width variation) directly the development of the three-dimensional flow structure, then to the erosional and depositional patterns, and then to the lateral migration patterns.

1 Introduction

Meandering rivers evolve and interact with floodplains for hundreds or even thousand of years (Latrubesse et al., 2005; Slowik, 2015; Almeida et al., 2016; Shan et al., 2018; Ielpi et al., 2018, 2021). They generally migrate laterally, upstream and downstream as their banks move due to fluvial erosion combined with mass failure processes (Langendoen, 2000; Motta et al., 2014). In fact, meandering patterns get more complex due to the influence of external forcing processes associated, for instance, with groundwater, vegetation, climate and geology. Evidence of this complex evolution of meandering rivers is given by the observed natural sedimentary architecture (Jackson, 1976; Shan et al., 2018) and by the artificially reproduced (via experimental and/or numerical work) records (Motta et al., 2012; Guneralp & Marston, 2012; Motta et al., 2014; Langendoen et al., 2016).

As regards river geomorphology, Seminara (2010) defined as free patterns those arising spontaneously from the water-sediment interaction, such as bed forms and river planforms, while forced patterns are those erosional/depositional patterns that are triggered by external factors such as changes in hydrology- and hydraulic-driven boundary conditions. Considering the free patterns, Colombini et al. (1992) stated that sediment bars are the product of flow and sediment coupling, and they control the morphology of alluvial channels, thus research has focused on the dynamics of alternate bars (bar instability) and river meandering (bend instability) (Garcia & Nino, 1993). Ikeda et al. (1981) stated that bar and bend instabilities operate at similar wavelengths when the sinuosity is not too large. Colombini et al. (1987) estimated the finite amplitude of alternate bars in straight channels under steady flows (for unsteady flows, see Hall (2004); to include the effects of suspended sediment on alternate bars, see Bertagni & Camporeale (2018)), and described the instability phase diagram for the presence of alternate bars ($\beta > \beta_C$, where β is the half width-to-depth ratio $= B^*/H_0^* =$ half-width/water depth and β_C is the critical value). In this paper, notations with an asterisk indicate quantities with dimensions, while notations without an asterisk denote their dimensionless counterparts. Kinoshita & Miwa (1974) performed experiments in a meandering channel with wavelength expected to produce alternate bars, and observed the critical condition (angle between channel centerline and down-valley direction between 20 and 40 degrees) under which alternate bars are suppressed (due to planform curvature effects). Tubino & Seminara (1992) developed a theoretical approach to estimate the threshold value for bar suppression, and Seminara & Tubino (1992) confirmed that (at the nonlinear level) at resonance condition (when bar and planform instabilities coincide by having similar wavenumbers, and consequently the erosional and depositional patterns reach their maximum magnitude producing stable geomorphic patterns), curvature forces a natural response of the channel consisting of steady non-migrating bars. However, as pointed out by Kinoshita (1961) and verified later by Whiting & Dietrich (1993b,c,a), migrating bars are again observed for the case of high-amplitude and high-curvature bends, thus leading to more complex planform dynamics as described by Hickin (1974).

Blondeaux & Seminara (1985) developed a unified bar-bend theory of river meanders, where the concept of resonance between free and forced bars was introduced. The resonance condition (β_R) was said to control bend growth, and the range under which resonance occurs is related to stable (non-amplifying) bar perturbations. Later on, Zolezzi & Seminara (2001) presented the exact solution for the linear problem of meander morphodynamics, however, in their derivations they did not consider the effect of migrating bars in high-amplitude bends as described by Whiting & Dietrich (1993b,c,a). They stated that the presence of migrating bars would tend to enhance the process of bank erosion, but the essential characteristics of meander development would remain, due to time scale differences. Lanzoni & Seminara (2006) analyzed the implications of having convective or absolute bend instability on a meandering channel. In the convective type, any nonpersistent perturbation incorporated into the system will be transported downstream leaving the domain. In the absolute type, any perturbation will spread upstream and downstream, disrupting the entire domain. The threshold condition at which convective or absolute instabilities occur in a meandering channel is given by the resonance half width-to-depth ratio condition (β_R) (Blondeaux & Seminara, 1985). The sub-resonant regime is defined by having low values of hald width-to-depth ratio compared to the resonant threshold ($\beta < \beta_R$). The super-resonant regime is defined by high values of half width-to-depth ratio ($\beta > \beta_R$).

Zolezzi et al. (2005) stated that bed topography in curved channels is the outcome of the interaction between free (migrating) and forced (non-migrating) patterns, which were previously investigated experimentally by Kinoshita & Miwa (1974) and theoretically by Tubino & Seminara (1992) for the case of small-amplitude periodic meanders, where linear models are still valid. However, the case of high-amplitude high-sinuosity bends (experiments: Whiting & Dietrich (1993b)) still remains as evidence of an instance where bars are not suppressed by curvature effects. Zolezzi et al. (2005) performed experiments in a U-type channel (long straight reaches at the upstream and downstream ends, with a 180 degrees bend in the middle reach). These experiments were carried out under sub- ($\beta < \beta_R$) and super-resonant ($\beta > \beta_R$) conditions. Zolezzi et al. (2005) found that downstream (upstream) overdeepening is observed for the sub-resonant (super-resonant) condition. Thus, depending on the location along the bend, a steady (non-migrating) pattern for overdeepening (based on the morphodynamic regime) is observed. Seminara et al. (2001) and Monegaglia et al. (2019) have discussed that for sub-resonant morphodynamic conditions, rivers tend to have upstream-skewed bends, while for the super-resonant morphodynamic conditions, the bends are downstream-skewed. Guo et al. (2019) argued that low-sinuosity bends tend to be downstream-skewed, while high-sinuosity bends (>2.6) tend to be upstream-skewed (as observed by the orientation of oxbow lakes). However, Guo et al. (2019) did not explain the underlying processes of this transition from downstream- to upstream-skewed bends when sinuosity increases and what is the role of morphodynamic regimes on bend orientation.

Abad & Garcia (2009a) have analyzed the effect of bend orientation on the hydrodynamics of Kinoshita curves (Parker et al., 1983; Parker & Andrews, 1986). Abad & Garcia (2009a) stated that the core of maximum velocity is located at the inner bank under flat-bed conditions, however when adding sediments (Abad & Garcia, 2009b), the core of maximum velocity shifts towards the outer bank due to the depositional processes (accretion) at the inner bank. Abad & Garcia (2009b) performed experiments for low half width-to-depth ratio ($\beta = 2$, no presence of migrating bars, but migrating dunes were observed) and described that when the bend is downstream-skewed, the bed morphology is more developed, having larger dunes promoting excess shear stresses along the outer bank, thus enhancing fluvial bank erosion (Abad et al., 2013). Bed alluvial topography in subaerial meandering channels is governed by the interaction of macroform (dunes: scaling with water depth, bars: scaling with channel width) and microform (ripples: scaling with the turbulent boundary layer) morphological structures, thus, the local hydrodynamics and bed morphodynamics are continuously affected by this interaction (Abad & Garcia, 2009b), and external forcing factors may further add to the complexity of this interplay. Indeed, as observed by Parsons et al. (2005),Dinehart & Burau (2005), and Konsoer et al. (2016), macroforms and microforms are constantly migrating, thus, a pulsating type of excess shear stresses might be exerted along the outer river banks (Abad et al., 2013).

In this study, insights on the hydrogeomorphology of US- and DS-skewed bends are presented, based on a combination of experimental and field measurements. As discussed before, Abad & Garcia (2009b) described the steady and fluctuating components of bed morphology for the case of migrating dunes (low β, where bars are not observed); herein, a set of experiments are presented for sub- and super-resonant conditions in the asymmetric Kinoshita channel to observe the resulting bed morphology in the presence of migrating bars, thus covering a wider range of half width-to-depth ratios. Then, field measurements of the hydrodynamics and bed morphodynamics of the Tigre River (a tributary of the Marañón River in Peru) are presented. The Tigre River was selected based on: 1) currently low lateral migration rates, associated with an expected preservation of planform shape, thus this study can focus mainly on hydrodynamics and bed morphodynamics of asymmetric bends and neglect planform migration rates (as opposed to other Amazonian rivers such as the Ucayali River (Abad et al., 2022)); 2) currently low sediment transport rates, thus bedforms are well developed and preserved (for proper discrimination of bedforms); 3) the river contains a reach where upstream and downstream oriented bends (of different levels of skewness) are observed within the same geological setting (avoiding heterogeneous geological conditions); 4) the reach is not affected by tributaries that could modify flow and sediment fluxes; and 5) substantially uniform sediment size distribution is observed along the studied reach. As observed in Figure 1A, the river is characterized by a narrow geological valley where meanders are developed and paleochannels are observed, mostly along the upstream and middle regions (Figures 1B and C). In the downstream region (Figure 1D), high amplitude bends are observed, two downstream-skewed [DS(LS) and DS(HS)] and two upstream-skewed [US(LS) and US(HS)] bends, where HS (LS) refers to high (low) skewness. Figure 1E shows the planform migration from 1990 to 2017 for bends DS(HS) and US(HS). Following Ruben-Dominguez et al. (2021)´s methodology, the planform statistics were extracted for the entire Tigre River (as shown by Figure 1). Figure 1F shows the number of bends plotted against different ranges of sinuosities (similar to Guo et al. (2019)), as well as the percentage of US-, DS-skewed, and compound bends. Indeed, based on this analysis, the percentage of US-skewed bends increases when sinuosity increases (the opposite occurs for DS-skewed bends). When sinuosity is less (larger) than 2.6, DS-skewed (US-skewed) bends are more common than US-skewed (DS-skewed) bends. Notice that the majority of bends have sinuosities less than 2.6. The underlying processes of how bends evolve from DS- to US-skewed dominated bends are still unknown. In the Tigre River, the low (high) flow occurs from November to February (May to July). Over geological time scales, the Tigre River has been active as part of the Pastaza River megafan, where several avulsive processes have occurred with the Corrientes and Tigre Rivers being located on the left side of the megafan (Bernal et al., 2011).

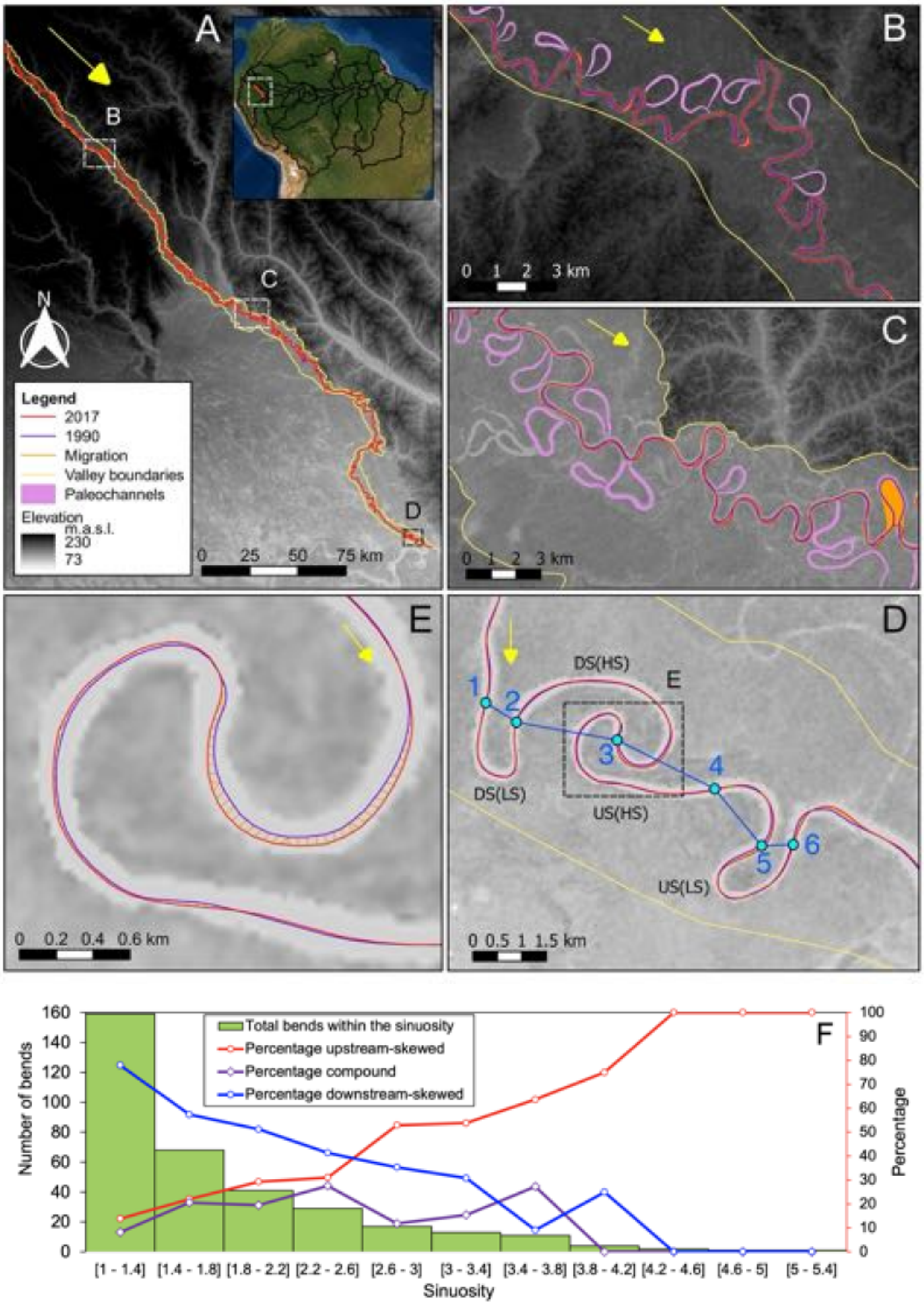

Figure 1. A: Tigre River, a tributary of the Marañón River (Peru), B: Upstream region, C: Middle region, D: Downstream region (two US- and two DS-skewed bends, the numbers from 1 to 6 identify the inflection points), E: Lateral migration vectors (from 1990 to 2017) for bends US(HS) and DS (HS), F: Statistics for bends along the Tigre River for the 2017 channel centerline. The satellite images were processed using CITA (2019, 2021) and Ruben-Dominguez et al. (2021)´s methodologies.

2 Experimental and field morphodynamic regimes

2.1 Experiments in the Kinoshita flume

A water and sediment recirculating flume known as the Kinoshita (based on Kinoshita curves, Parker et al. (1983); Parker & Andrews (1986)) flume (Figure 2) was used (Abad & Garcia, 2009a,b). The flume consists of three consecutive bends (Abad, 2005) to have both: 1) fully developed turbulent flow and 2) a fully developed secondary flow in the bends. The Kinoshita curves are expressed in intrinsic coordinates (s, n: where s is the streamwise coordinate and n is the transverse coordinate) as $\theta(s) = \theta_0 sin\left(\frac{2\pi s}{\lambda}\right) + \theta_0^3\left(J_s cos\left(3\frac{2\pi s}{\lambda}\right) - J_f sin\left(3\frac{2\pi s}{\lambda}\right)\right)$, where the angular amplitude θ is the angle between the local channel centerline direction and the down-valley direction, $J_s = \pm 1/32$ (+: upstream-, -:downstream-skewed oriented bends) and $J_f = 1/192$ are the skewness and flatness coefficients respectively, $\theta_0 = 110°$ is the maximum angular amplitude and λ is the arc wavelength (10 m). Notice that by reducing the magnitude of θ_0, the Kinoshita equation reduces to the well-known sine-generated symmetric curve (Leopold & Langbein, 1966), which was widely used in previous experiments (Whiting & Dietrich, 1993b,c,a). The channel width is 60 cm, and the total length of the flume is 32 m (1-m upstream straight reach, three bends of 10 m each, and 1-m straight reach at the downstream end). Sonar transducers were used to measure bed topography by placing them in a portable carriage that was moved from CS10 to CS20 (Figure 2). These measurements were performed after equilibrium conditions were reached (around 200 hours after initiation of experiments). Each experiment was repeatedly run for an hour, then slowly stopped for bed morphology measurements, and restarted. More details about the experimental setup, bed morphology and sediment transport measurements are found in Abad & Garcia (2009a,b); Abad et al. (2011).

2.2 Morphodynamic regimes in experimental and field conditions

In the absence of a fully nonlinear theory to define the critical and resonant condition for the interaction of free and forced bars, Blondeaux & Seminara (1985), Tubino & Seminara (1992), and Seminara & Tubino (1992)´s approaches were used to design the experiments and the resulting morphodynamic conditions in the Kinoshita channel. By using the two-dimensional Saint Venant equations, using Parker (1976)´s bedload predictor and following Colombini et al. (1987)´s approach, the supporting material describes

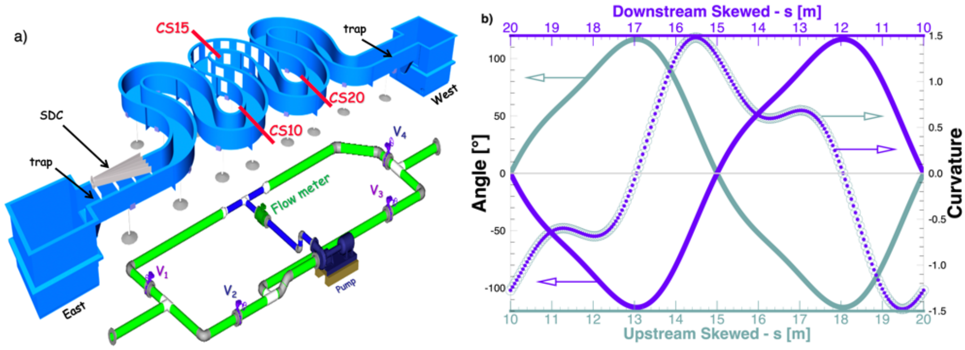

Figure 2. a) 3D view of the Kinoshita recirculating (water and sediment) meandering channel, b) the angular amplitude and channel curvature of the middle bend (CS10 to CS20). Notice that the peak of the curvature for the US- (DS-skewed) condition is closer to (farther from) the upstream inflection cross section CS13 (CS18).

the variation of the critical (β_C,λ_C) and resonant (β_R,λ_R) conditions for different values of Shield stress (τ^*) and non-dimensional sediment size (d_s). Then, considering the Kinoshita channel´s characteristics, the targeted (to cover the range of morphodynamic regimes) hydraulic conditions are obtained. The supporting material illustrates the effect of using different sediment size on the morphodynamic conditions (sub- and super-resonant), and it shows that the phase diagram corresponding to d_s^* ($= D_{s50}^*$) $= 0.832mm$ provides a wider range for experiments with presence of bars ($H_0^* = 2cm$, $H_0^* = 3cm$) and in absence of migrating bars ($H_0^* = 15cm$, where dunes are present) as those presented by Abad & Garcia (2009b). The phase diagram used to describe the experimental conditions is shown in Figure 3. There, if $\tau_C^* > \tau^*$, bars are expected to be formed ($\beta > \beta_C$), and when $\tau_C^* < \tau^*$ no bars are observed ($\beta_C < \beta$). If $\tau_R^* > \tau^*$ a super-resonant condition is expected ($\beta_R < \beta$), while for $\tau_R^* < \tau^*$ a sub-resonant condition is expected ($\beta_R > \beta$). Table 1 summarizes the experimental and field conditions.

2.3 Field measurements in the Tigre River

Figure 1 shows four bends, two with low skewness (LS) and two with high skewness (HS), each of them with upstream (US) or downstream (DS) orientation conditions. Table 1 shows the field conditions for three campaigns (September 2017 [transition], February 2020 [low-flow], and May 2021 [high-flow]). Field equipment included a RiverRay ADCP (Teledyne Ocean), coupled with an AtlasLink GNSS Smart Antenna, with global cor-

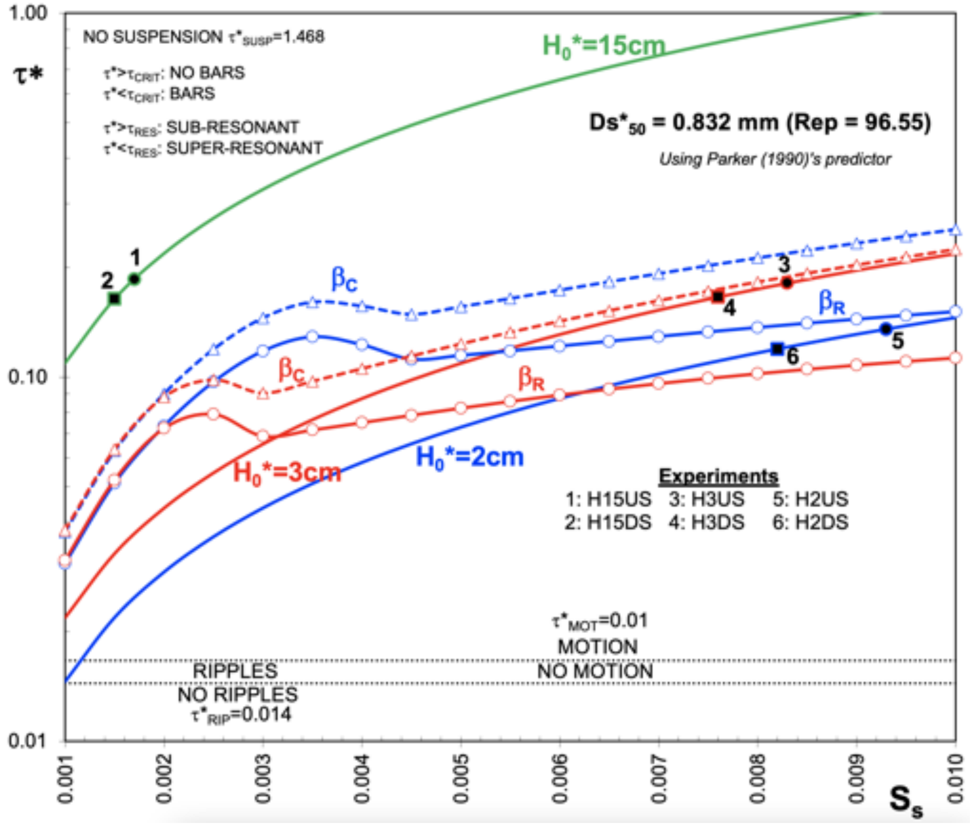

Figure 3. Phase diagram for the Kinoshita flume experiments under sub- and super-resonant regimes. $D^*_{s50} = 0.832mm$, τ^*: Shields stress, Re_p: Particle Reynolds Number, S_s: longitudinal water surface slope. US: Upstream-skewed, DS: Downstream-skewed. Notice that the critical (β_C) and resonant (β_R) curves are plotted for the designed experimental conditions. Numbers 1 to 6 denote the hydraulic conditions for the experiments in the Kinoshita channel.

Table 1. Summary of experimental and field conditions. Q_w^*: water discharge (experiments: $[lt/s]$, field $[m^3/s]$) (averaged over the measured cross sections), H_0^*: reach-averaged water depth $[m]$, S_S: longitudinal water surface slope, $u^* = \sqrt{gR_hS_S}$: reach-averaged shear velocity $[m/s]$ where R_h is the hydraulic radius, C_Z: Chezy friction coefficient ($C_Z = \frac{U_0^*\sqrt{g}}{u^*}$) where U_0^* is the reach-averaged flow velocity, $ds = \frac{d_s^*}{H_0^*}$: sediment ratio, $\tau^* = \frac{(u^*)^2}{Rgd_s^*}$: reach-averaged Shield stress, where R is the sediment submerged specific gravity, $\beta = \frac{B^*}{H_0^*}$: half width-to-depth ratio, β_R: resonance condition. *SubR*: Sub-resonant condition, *SupR*: Super-resonant condition.

Case	Q_w^*	H_0^*	$S_S(x10^{-3})$	$u*$	C_Z	ds	τ^*	β	β_R	*Condition*
H15US	25	0.15	1.7	0.041	6.80	0.0055	0.1858	2		SubR
H15DS	25	0.15	1.5	0.038	7.24	0.0055	0.1639	2		SubR
H3US	7.5	0.03	8.3	0.047	8.84	0.0277	0.1814	10	17.44	SubR
H3DS	7.5	0.03	7.6	0.045	9.24	0.0277	0.1660	10	16.63	SubR
H2US	3.5	0.02	9.3	0.041	7.05	0.0416	0.1355	15	13.89	**SupR**
H2DS	3.5	0.02	8.2	0.039	7.51	0.0416	0.1194	15	12.95	**SupR**
TSep17	1699	9.55	0.06	0.072	10.59	0.000036	1.02	12.2	91.32	SubR
TFeb20	1664	10.9	0.06	0.077	7.29	0.000031	1.17	12.5	105.75	SubR
TMay21	2880	13.54	0.06	0.084	10.63	0.000025	1.45	8.74	150.56	SubR

rection service (less than 10 cm). As described by Mueller & Wagner (2007) and Oberg & Mueller (2007), four transects were collected to describe the three-dimensional flow structure in each cross section, then the VMT software (Parsons et al., 2013) was used to describe the flow structure. A combination of multibeam iWBMS STX (Norbit), a receptor base, GR5 (Topcon), and the surveying and post-processing software Hypack Hysweep (Xylem) and PosPac MMS (Applanix) was deployed in the field to acquire the bed morphology data (February 2020).

3 Results

3.1 The experiments

Figure 4 shows the water surface elevation profile for the upstream- and downstream-skewed conditions in the Kinoshita channel. A linear fitted trend line was applied to the water surface profiles to obtain the water surface slopes (S_S, as reported in Table 1) and apparently US conditions tend to have slighter higher slope values than DS conditions.

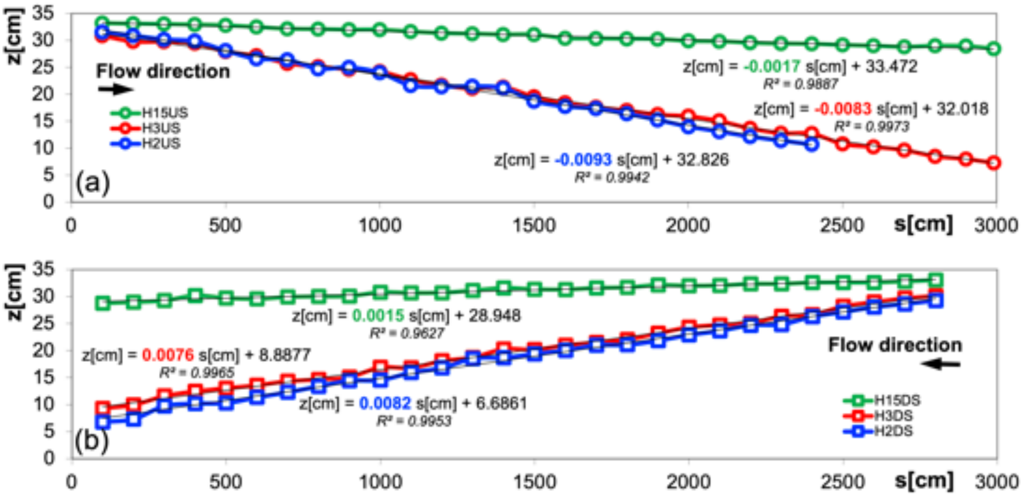

Figure 4. Water surface elevations and fitted linear trendlines along the channel centerline of the Kinoshita channel, a) US-skewed condition, b) DS-skewed condition. Measurements were carried out along the left and right banks of the channel, and the water surface elevation along the channel centerline was obtained performing an arithmetic average. For super-resonant conditions, higher slopes are observed than those for sub-resonant conditions. For US-skewed conditions, slightly higher slopes are found compared to DS-skewed conditions. Note: for the experiment H2US, water surface elevations were not recorded for the last stations ($> 2400cm$).

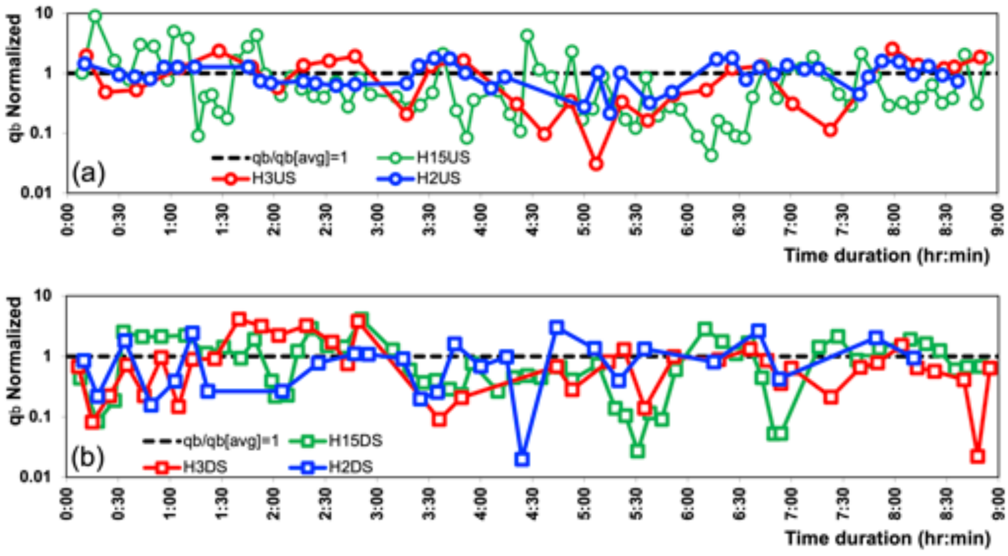

Figure 5. Normalized (using time-averaging) bedload sediment discharge in the Kinoshita channel, a) US-skewed condition b) DS-skewed condition. Sediment transport measurements were carried out over a period of approximately 9 hours after reaching dynamic equilibrium conditions.

Similarly to (Abad & Garcia, 2009b), bedload sediment transport measurements (see Figure 5) were carried out using the sediment trap located at the outlet of the Kinoshita channel. These measurements show that there is a fluctuating sediment pulse changing in time, mainly due to bedform migration. Notice that the Kinoshita experiments were carried out in a recirculating (water and sediment) setup, where the averaged sediment load is transported on the steady bed morphology and also by the fluctuating contribution of the migrating bedforms (bars, dunes and ripples). In general, rivers behave like the Kinoshita channel, where even though there might be a constant water discharge, the sediment discharge changes in time due to bedform migration. In the following sections, the experiments are described with reference to the middle bend of the Kinoshita channel (CS10 to CS20, see Figure 2).

3.1.1 H15US and H15DS

Figure 6 shows the bed evolution (T=1 to 6 hours) for the US- and DS-skewed conditions for $H_0^* = H_{15}$=15cm. As described by Abad & Garcia (2009b), the DS-skewed condition produces more developed bedforms since the planform configuration (see angular amplitude and curvature for DS-skewed condition, Figure 2) promotes the development of stronger secondary flow cells and therefore more pronounced erosional/depositional patterns, as described by Abad et al. (2013). Abad & Garcia (2009b) also observed that the DS-skewed condition produces more bedforms (from CS17.5 to CS13) than the US-skewed condition (from CS14 to CS17.5). Bedforms are preferentially dunes of different sizes, and no migrating bars were observed. The DS-skewed condition produces higher bedform roughness values compared to the US-skewed condition.

3.1.2 H3US and H3DS

Figure 7 shows the bed evolution (T=1 to 6 hours) for the US-skewed and DS-skewed conditions ($H_0^* = H_3$=3cm). As illustrated in Figure 2, the peak of the curvature for the US- (DS-skewed) condition (around CS14.5) is closer to (farther from) the upstream inflection point (CS13 for US condition and CS18 for DS-skewed condition). As a consequence, for the DS-skewed condition, there is a longer distance where flow and bed morphology (including bedform patterns) might get more developed. Indeed, for the US-skewed condition, between CS13 and CS14 there is an evident change of sediment deposition from left to right bank (produced by the change in curvature), and the peak of the curvature

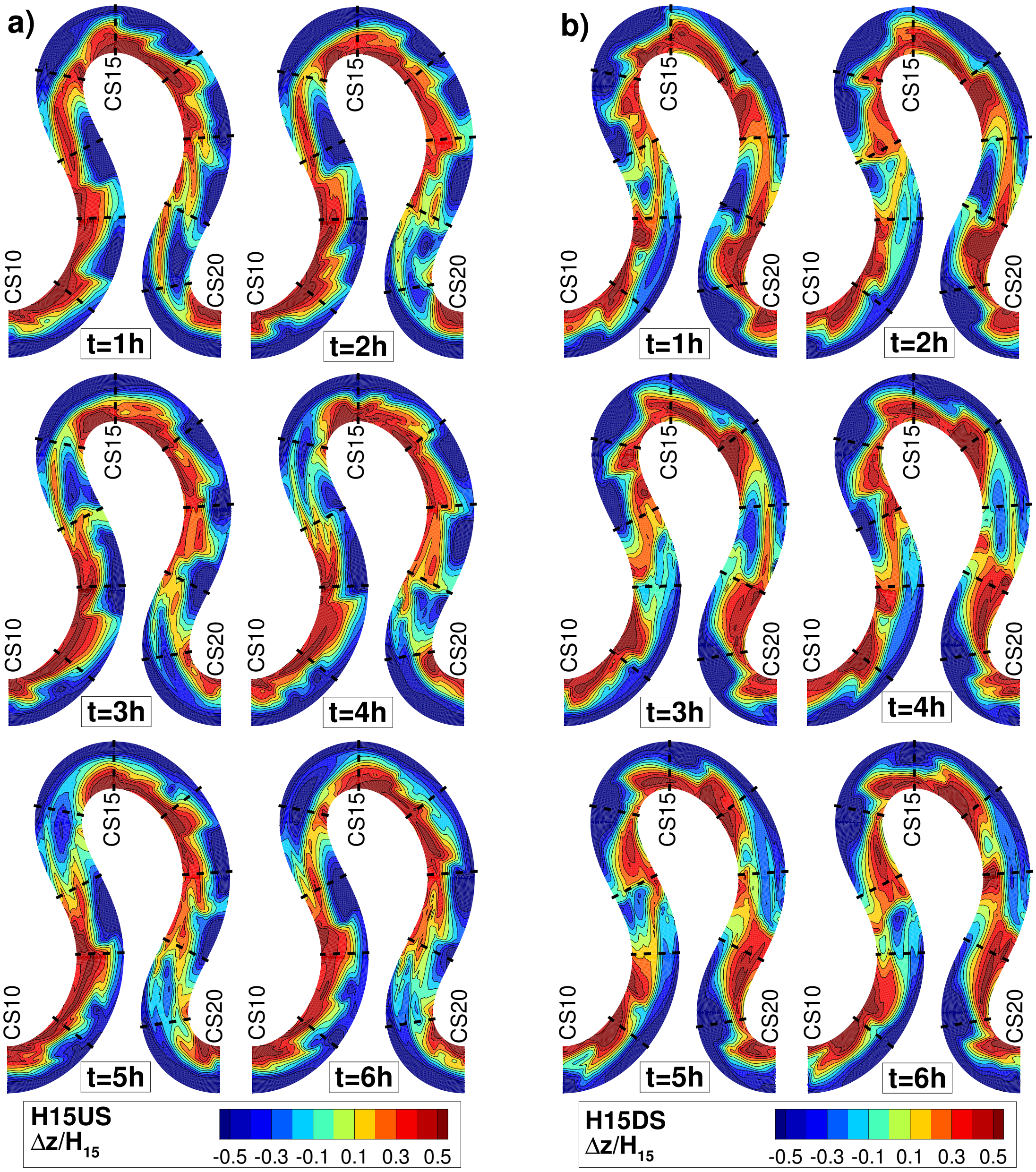

Figure 6. Normalized bed elevations for $H_0^* = H_{15}$=15cm, a) US-skewed condition (flow from left to right), b) DS-skewed condition (flow from right to left). $\Delta z = z(cm) - < z_{CS15} >$, where $< z_{CS15} >$ is the average of the bed elevations in CS15. The middle bend of the Kinoshita channel (from CS10 to CS20) is shown. Similar data was presented in Abad & Garcia (2009b).

occurs just downstream (at CS14.5, where also the highest deposition at the inner bank happens), and after that location, bars tend to develop. On the contrary, for the DS-skewed condition, the change of sediment deposition between banks (from right to left) happens between CS18 to CS17, and bars start to form and they are already mature when arriving to the location with the highest planform curvature (CS14.5). For the DS-skewed condition, there is a significant deposition zone near the inner bank around CS16.

3.1.3 H2US and H2DS

Figure 8 shows the bed evolution (T=1 to 6 hours) for the US- and DS-skewed conditions ($H_0^* = H_2$=2cm). Similarly to the H3US and H3DS experiments, for the US-skewed condition, there is a significant depositional zone near the highest curvature location (CS14.5), while the depositional zone for the DS-skewed condition, larger than for the US-skewed condition, is located near CS16.5. For the DS-skewed condition, there is a drastic change of the bathymetry from one side to the other, as the flow tends to be concentrated near the outer banks.

3.1.4 Time-averaged bed morphology

Figure 9 shows the normalized time-averaged bed morphology for all experiments (US- and DS-skewed conditions). For all experiments, the inflection point is at CS13 and CS18 for US- and DS-skewed condition respectively and the change of erosional/depositional pattern between banks occurs with a lag between 0.25m to 0.5m (comparable with the channel width = 0.6m). Comparing the H_3 and H_2 experiments for the US and DS-skewed conditions, the depositional zone near the inner banks shifts slightly upstream for the super-resonant condition (H_2), as suggested by Zolezzi et al. (2005). For the US- and DS-skewed conditions the highest erosional zone is located around the highest curvature point (CS14.5), therefore, bends (if allowed) might continue migrating maintaining their planform configurations (at least at high amplitude conditions). Based on the steady bed morphology, the inner bank depositional area is larger for the DS- than the US-skewed condition. The transversal bed slope for H_{15} is approximately constant across the entire channel width, while, for the H_3 and H_2 experiments, there is a more pronounced depositional point bar and and an abrupt change in transversal bed slope close to the outer bank, thus the flow is mostly concentrated in the outer bank.

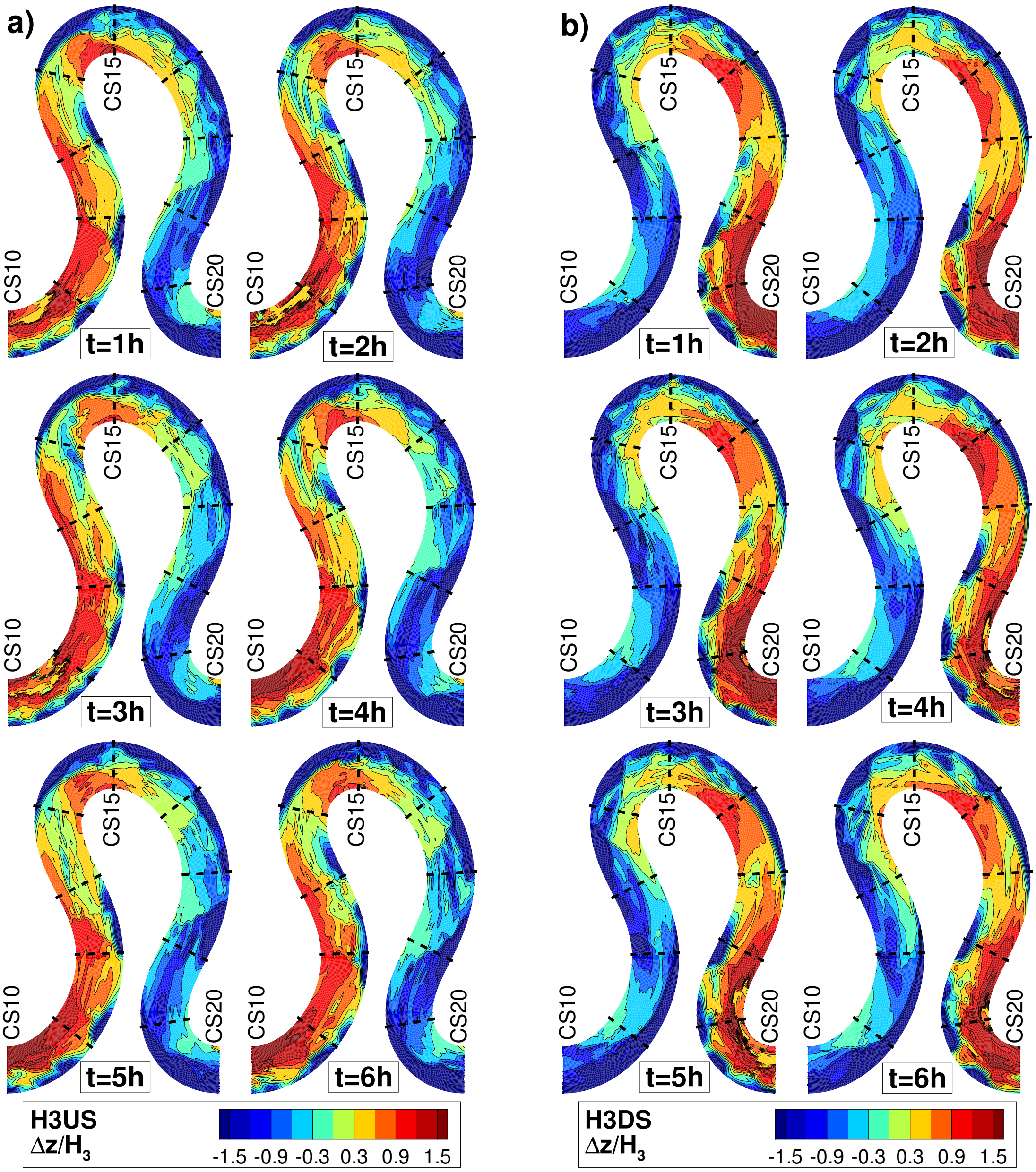

Figure 7. Normalized bed elevations for $H_0^* = H_3$=3cm, a) US-skewed condition (flow from left to right), b) DS-skewed condition (flow from right to left). $\Delta z = z(cm) - < z_{CS15} >$. The middle bend of the Kinoshita channel (from CS10 to CS20) is shown.

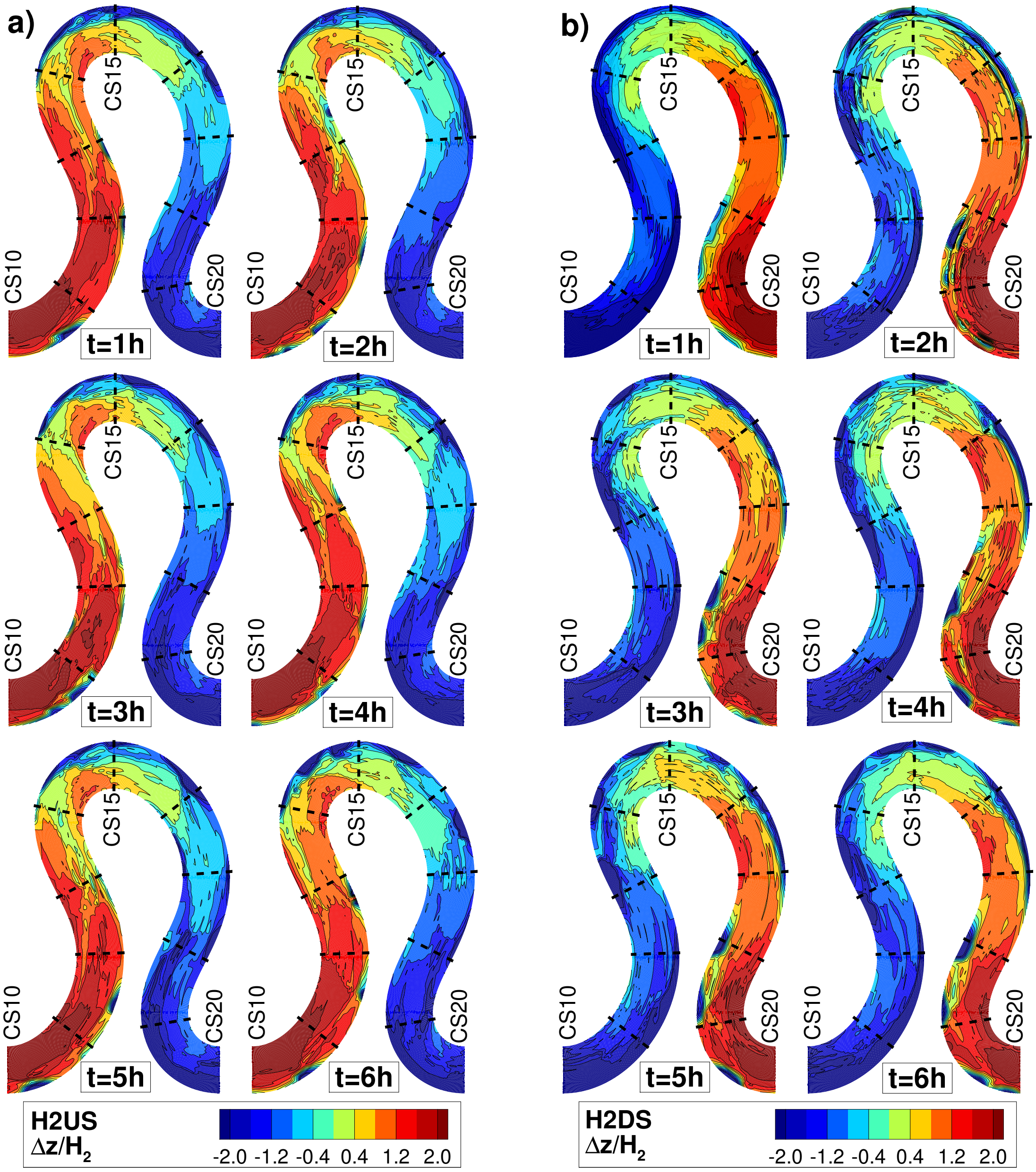

Figure 8. Normalized bed elevations for $H_0^* = H_2$=2cm, a) US-skewed condition (flow from left to right), b) DS-skewed condition (flow from right to left). $\Delta z = z(cm) - < z_{CS15} >$. The middle bend of the Kinoshita channel (from CS10 to CS20) is shown.

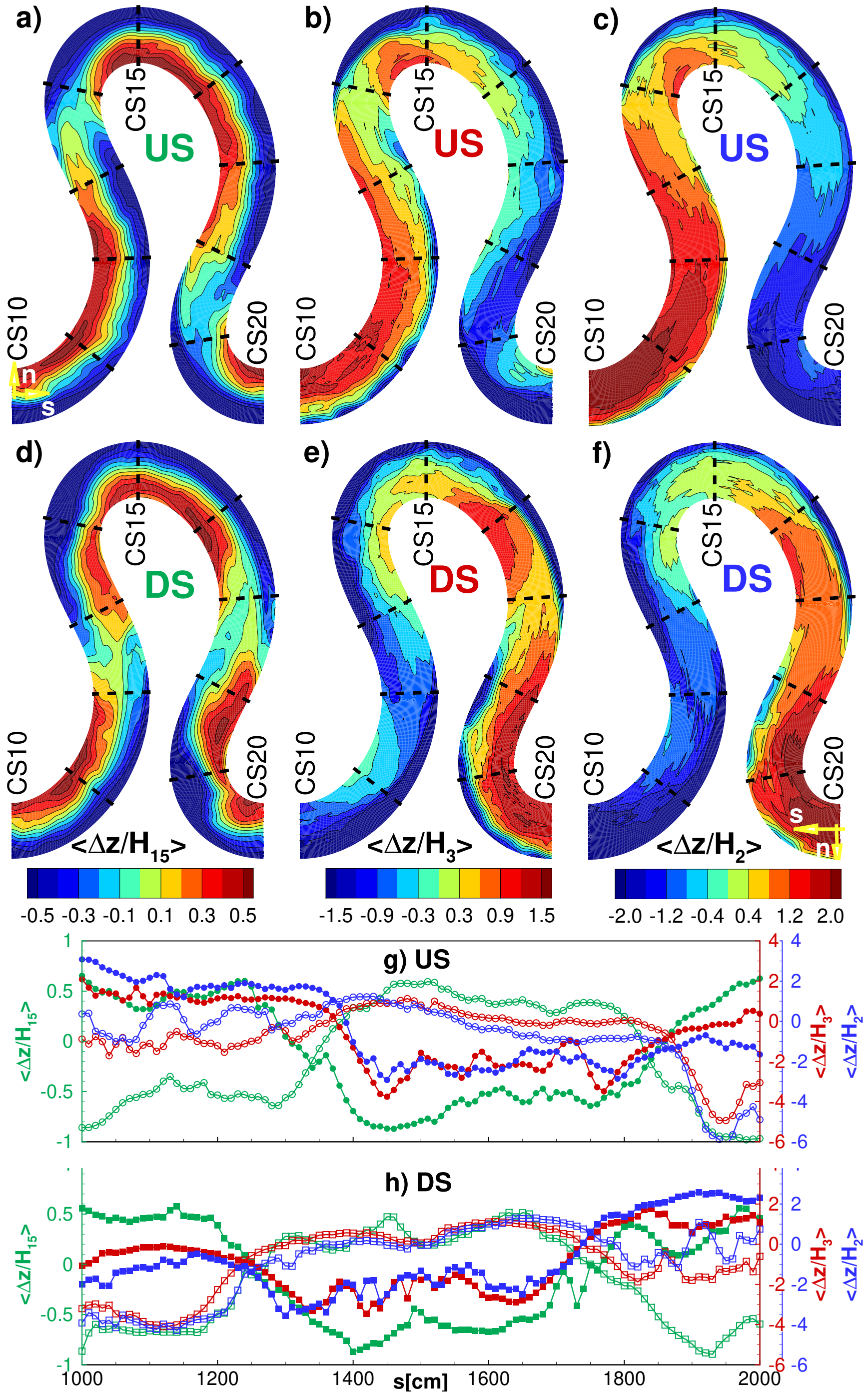

Figure 9. Normalized time-averaged bed morphology (from T=1 to T=6 hours). US-skewed condition (flow from left to right): a) H_{15}=15cm, b) H_3=3cm, c) H_2=2cm. DS-skewed condition (flow from right to left): d) H_{15}=15cm, e) H_3=3cm, f) H_2=2cm. Normalized averaged bed morphology along the channel banks: g) US-skewed condition: left [n=30] (right [n=-30]) bank is with filled (empty) circles, h) DS-skewed condition: left [n=30 cm] (right [n=-30 cm]) bank is with empty (filled) circles, $\Delta z = z(cm) - < z_{CS15} >$.

3.2 The field measurements in the Tigre River

3.2.1 High-resolution bed morphology

Figure 10 shows the multibeam measurements of the Tigre River that include two US-skewed (LS and HS) and two DS-skewed (LS and HS) bends. For the DS-skewed(LS) bend, the deepest scour hole near the outer bank is located between cross sections S3, S4 and S5, where the highest curvature is also observed (similar pattern to the DS-skewed laboratory experiments). For the DS-skewed(HS) bend, the deepest scour covers a longer portion of the bend (from S9 to S12-S13), showing that DS-skewed bends tend to produce longer scour holes along the outer bank. The transition from DS-skewed(HS) to US-skewed(HS) occurs within a very short distance (around S13), nonetheless the bed morphology rapidly shifts and for the US-skewed(HS) bend, the outer bank scour hole is located between S13, S14 and S15. Channel narrowing occurs along the US-skewed(HS) bend around SE and SF, including a slight change of channel curvature. Further downstream in US-skewed(HS), due to the curvature, a long outer bank scour hole is observed (S15 to S20). For the US-skewed(LS) bend, the outer bank scour hole is located between S24 and S27 approximately. Figures 10b, c, and d show details of the bed morphology along low sinuosity reaches, where bedforms are composed of dunes and ripples of different size. It seems that curvature effects drastically modify incoming well-developed bedforms as they enter bends.

Figure 11 shows repeated (ranging from 0.5h [P2] to 25h45m [P4,P5]) multibeam measurements along six longitudinal profiles carried out in February 2020 in order to characterize bedforms and estimate bedload sediment transport rates. As observed even for the longest time interval of 25h45min (P4 and P5 profiles), the change in bed morphology is not as dynamic (translation of 1m for P4 profile, 0.40 ton/m/day of bedload sediment rate) as other meandering rivers such as the Ucayali River(Abad et al., 2022; Guerrero et al., 2022). After discrimination (using Gutierrez et al. (2013, 2018)´s techniques), dune characteristics are in general smaller than 10m in arc-wavelength and 0.5m in amplitude, except P5 that is characterized by 56.3m arc-wavelength and 1.5m amplitude. All profiles are located in bends, except for P1 and P5, thus confirming that the dune characteristics along low sinuosity reaches (see Figure 10b, c and d) are larger than those under curvature forcing, where bedforms structures are interacting with more steady structures (e.g. point bars).

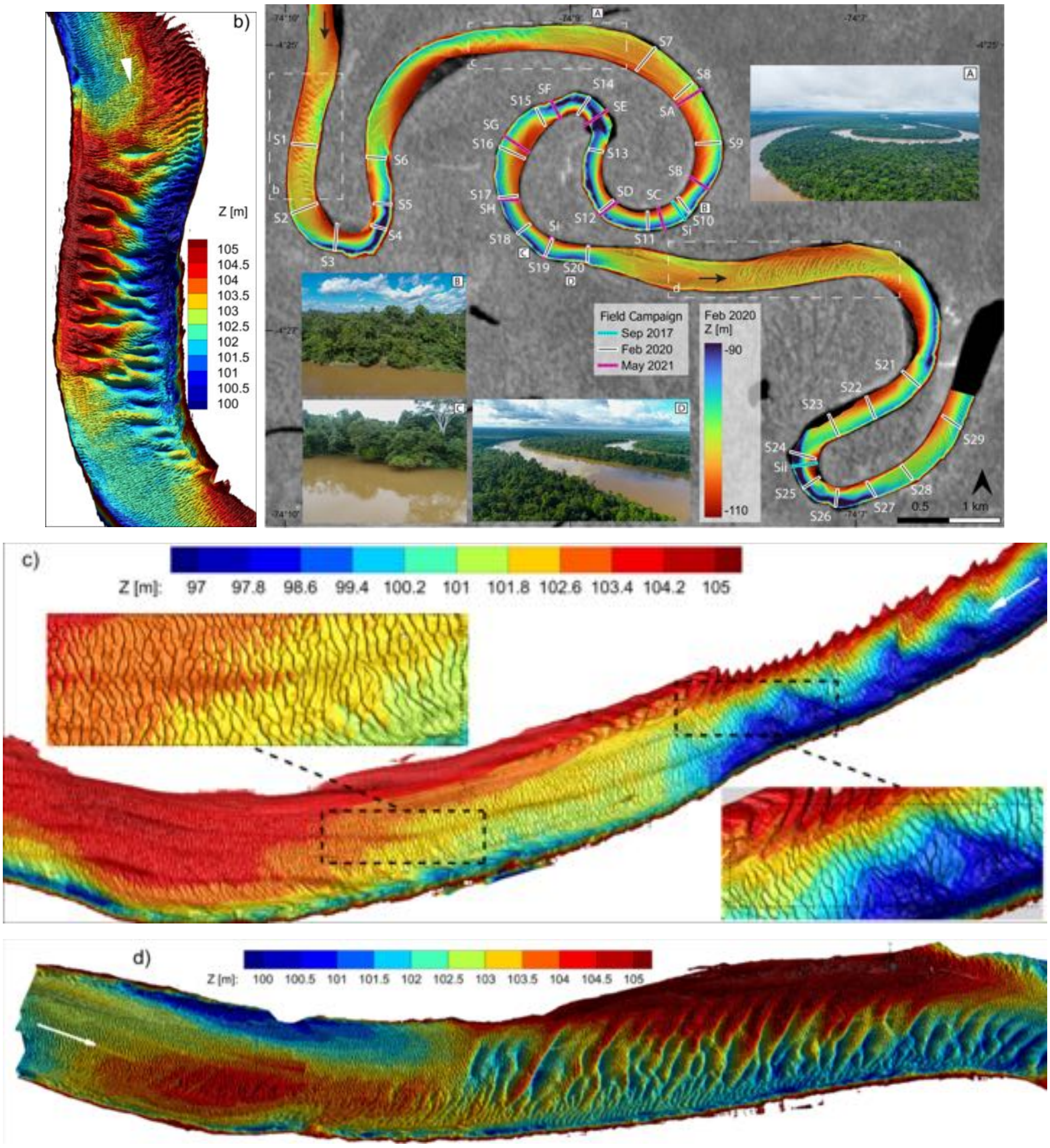

Figure 10. a) Bed morphology measurements (using multibeam, bed elevation in m.a.s.l) along the Tigre River. Figures b), c) and d) show low sinuosity reaches with presence of bedforms. With reference to Figure 1, upstream-oriented bends are located between S12-S13 and S20 for US(HS) and from S21 to S29 for US-skewed(LS) bend; downstream-oriented bends are located between S1 and S6 for DS-skewed(LS), and from S7 to S12-S13 for DS(HS). *LS*: Low skewness, *HS*: High skewness. A, B, C and D are pictures from the field campaigns.

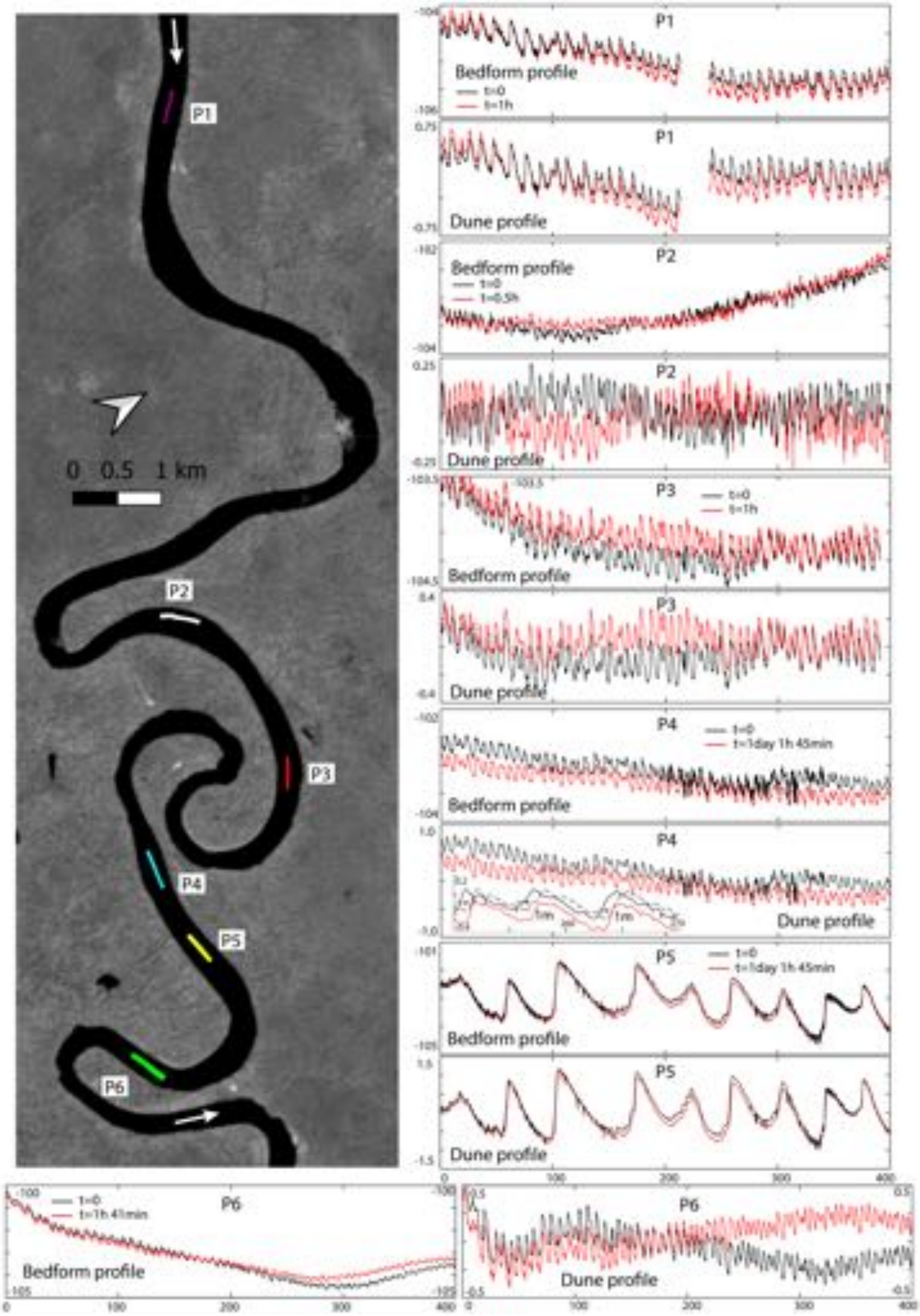

Figure 11. Repeated multibeam measurements along six longitudinal bedform profiles (elevation in m.a.s.l.). Dune profiles (in m) were obtained using discrimination techniques provided by Gutierrez et al. (2013, 2018). P1 is located in a low-sinuosity reach further upstream from the studied bends. Notice that P5 does not need detrending from bars since it is located along a low-sinuosity channel where curvature forcing is not significant.

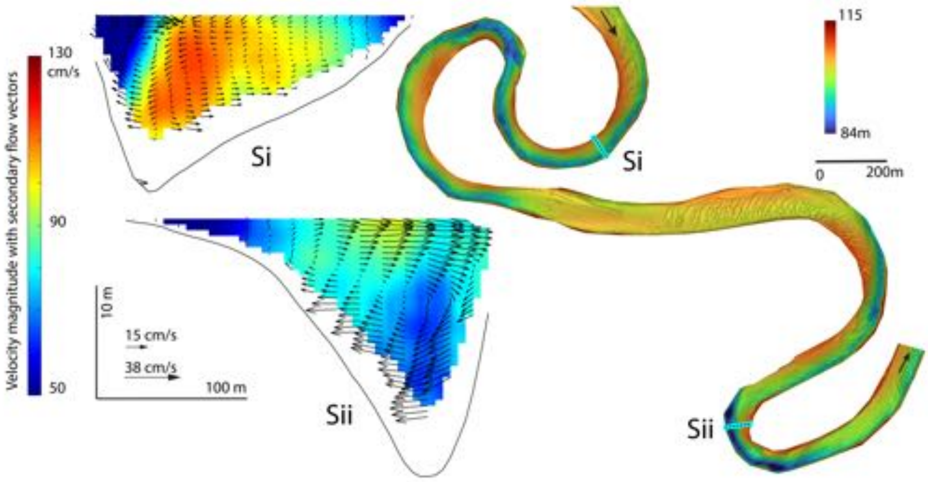

Figure 12. September 2017: ADCP-based flow velocity measurements at cross sections Si and Sii. $Q_w = 1699m^3/s$ (averaged [over the entire campaign] water discharge).

3.2.2 September 2017´s hydrodynamic measurements

Figure 12 shows the velocity magnitude and secondary flow for September 2017 at cross sections Si (between S10 and S11, DS-skewed(HS) bend) and Sii (between S24 and S25, US-skewed(LS) bend). The core of high velocity at Si is located between the middle and outer bank regions (due to the influence of the main channel narrowing downstream of SB and upstream of Si), showing a very well developed counter clockwise secondary flow. For Sii, the cross section is bigger (wider and deeper) than at Si, thus the velocity magnitude is reduced, however the clockwise secondary flow is very well developed. Comparison of flow velocity distribution in Si and Sii shows that small variations in channel width and depth significantly can influence secondary flows and velocity magnitudes.

3.2.3 February 2020´s hydrodynamic measurements

Figure 13 shows the flow structure along the DS-skewed(LS) bend for February 2020. At S1, the flow is exiting the low sinuosity channel (see Figure 10b), thus the core of the velocity magnitude is located around the middle portion of the cross section and the intensity of the secondary flow is very weak. Further downstream, at S2, there is a clockwise secondary flow that is enhanced at S3 and S4. At S4 (located slightly downstream from the bend´s highest curvature location), the outer bank scour hole is very deep and

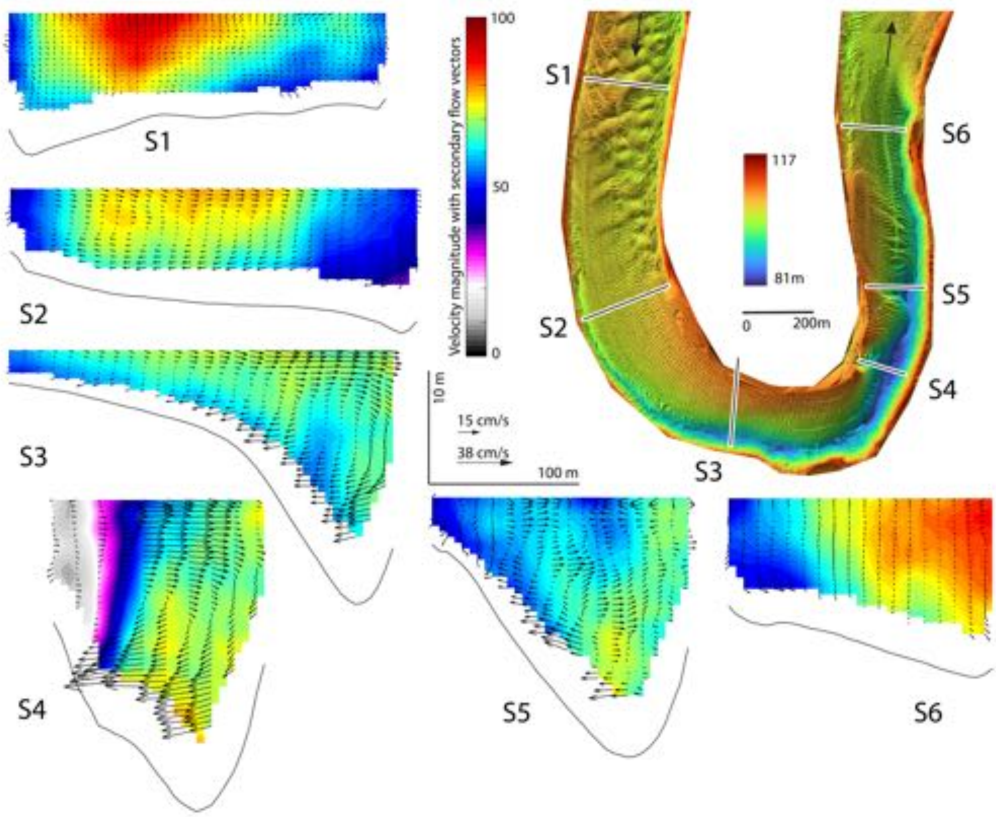

Figure 13. February 2020: ADCP-based flow velocity measurements along DS-skewed(LS) bend (cross sections can be found in the bathymetry figure). $Q_w = 1664 m^3/s$ (averaged [over the entire campaign] water discharge).

the secondary flow is the strongest along the bend (as well as the transverse bed slope). At S5, the secondary flow loses its coherence with an interaction of different cells (one clockwise close to the bed and another one counter clockwise near the water surface). By observing the bathymetric measurements, S5 is located just downstream of a large bedform, thus the expected secondary flow is disrupted by the presence of the bedform (similar to Abad et al. (2013)). S6 is located in a low sinuosity channel, thus the secondary flow is weak, however the planform curvature from upstream still has its influence because the bed elevation near the right bank is slightly lower than the bed elevation near the left bank.

Figure 14 shows the flow structure at the DS-skewed (HS) and US-skewed(HS) bends. From S7 to S13, the secondary flow has a counter clockwise orientation, while the secondary flow reverses (clockwise) from S14 to S20 due a drastic change in planform curvature. The channel width for the DS-skewed (HS) bend is slightly larger than the US-skewed(HS) bend (except between S15 to S16 for the US-skewed bend), thus the velocity magnitude is smaller along the DS-skewed bend. Note that S14 and S15 were measured on a different date when water discharge was smaller, consequently at S14, where there is a deeper scour hole, smaller water velocity magnitudes were observed.. Well developed point bars are observed for both DS-skewed (HS) (from S8 to S12) and US-skewed(HS) (from S15 to S19), with a wider depositional zone between S8 and S9.5 and from S15 to S16.5 for the DS- and US-skewed bend, respectively.

Figure 15 shows the flow velocity distribution for the US-skewed(LS) bend, where there is an incoming secondary counter clockwise flow (produced by the upstream bend), however, due to the change in curvature around S24 (highest curvature along the bend), the secondary flow reverses until S27, being dissipated almost completely at S28 and appearing again due to another slight change in curvature at S29. The deepest outer bank erosion hole is located between S24 and S26. At S24, the cross section is wider and deeper reducing the flow velocity compared to other sections.

3.2.4 May 2021´s hydrodynamic measurements

Figure 16 shows the flow structure for the DS-skewed (HS) and US-skewed(HS) bends for the May 2021 campaign. SE is located between S13 and S14, and the deepest scour hole is located around the mid channel, where the high core of velocity magnitude is ob-

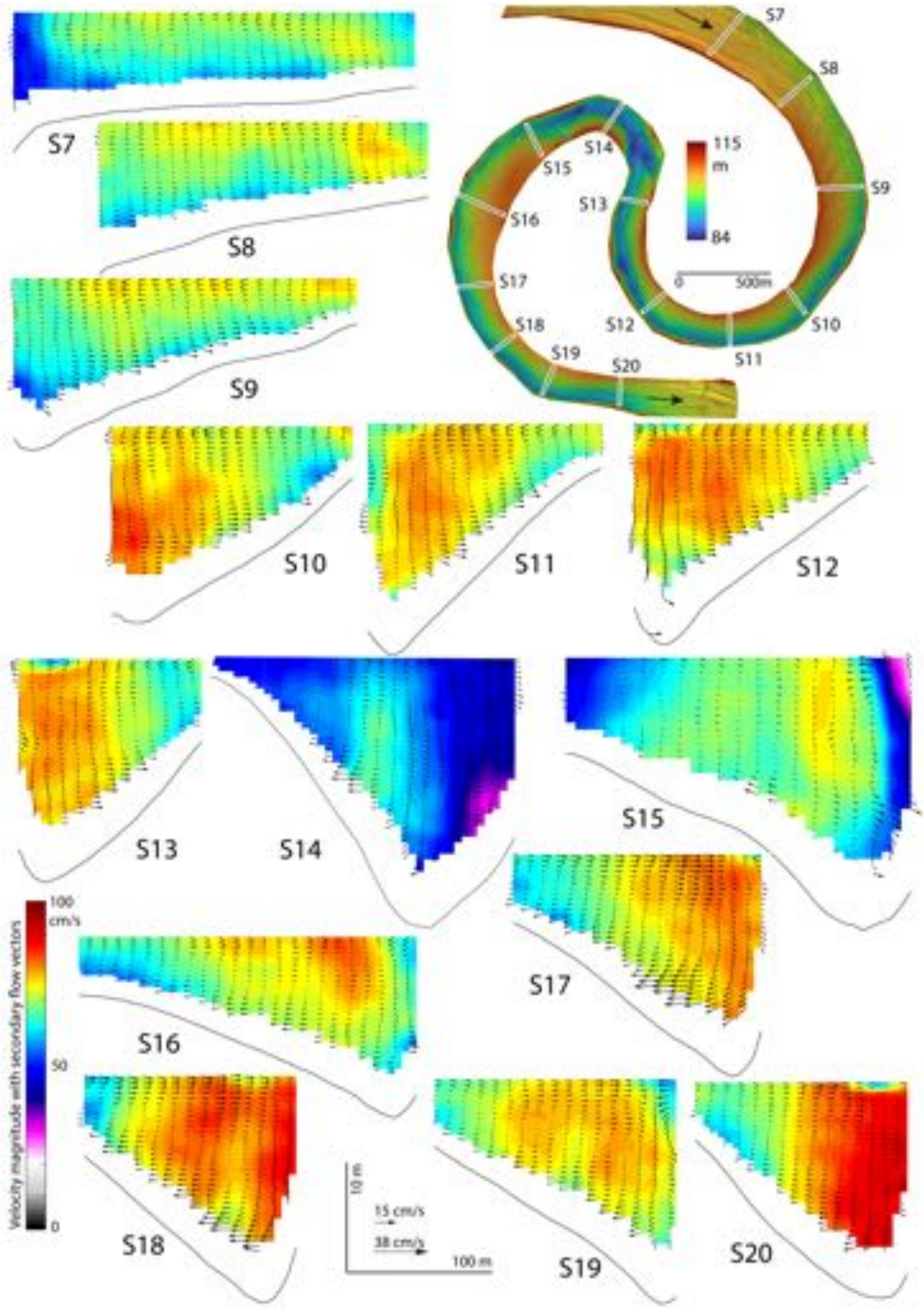

Figure 14. February 2020: ADCP measurements along the DS-skewed (HS) and US-skewed(HS) bends. $Q_w = 1664m^3/s$ (averaged [over the entire campaign] water discharge). $Q_w = 1477m^3/s$ (S14, S15), $Q_w = 1626m^3/s$ (S7-S13), $Q_w = 1781m^3/s$ (S16-S20).

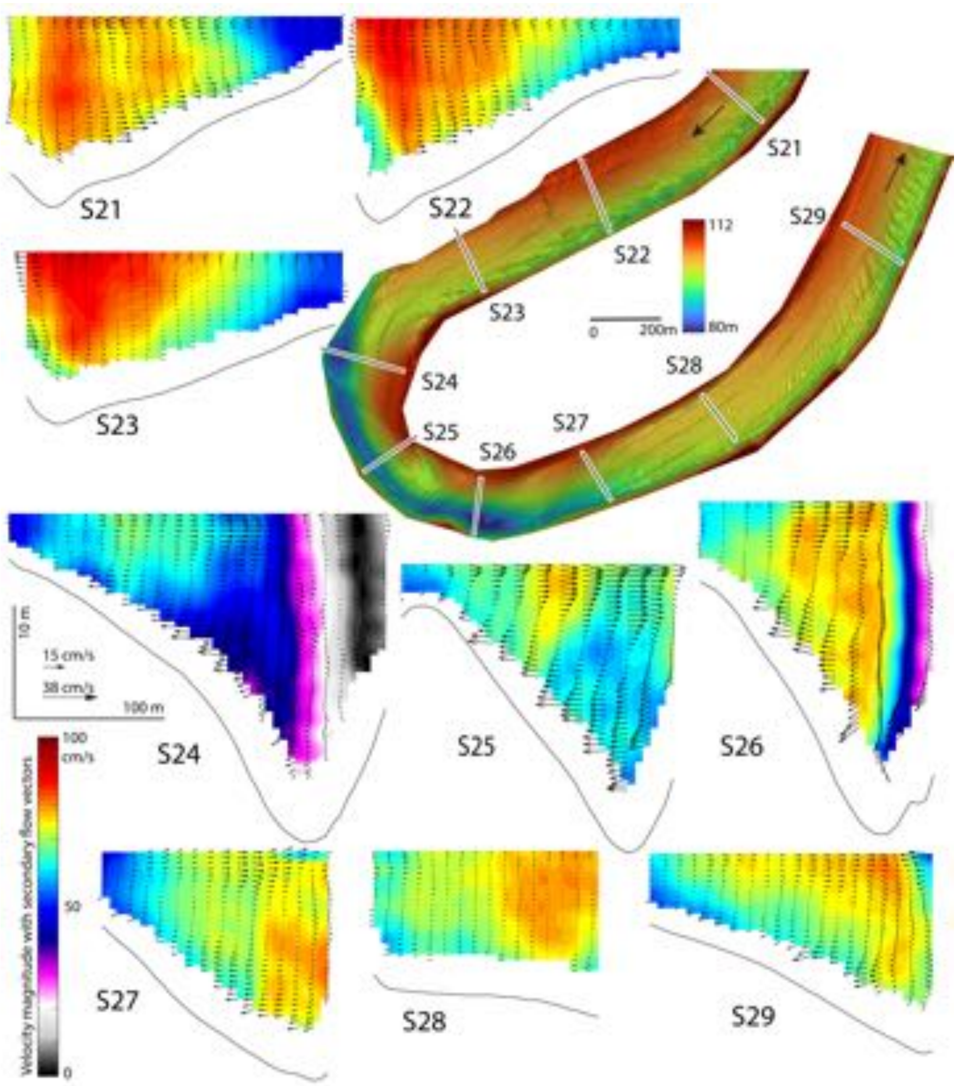

Figure 15. February 2020: ADCP measurements along the US-skewed(LS) bend. $Q_w = 1664m^3/s$ (averaged [over the entire campaign] water discharge). $Q_w = 1477m^3/s$ (S24), $Q_w = 1781m^3/s$ (S21-S23, S25-S29).

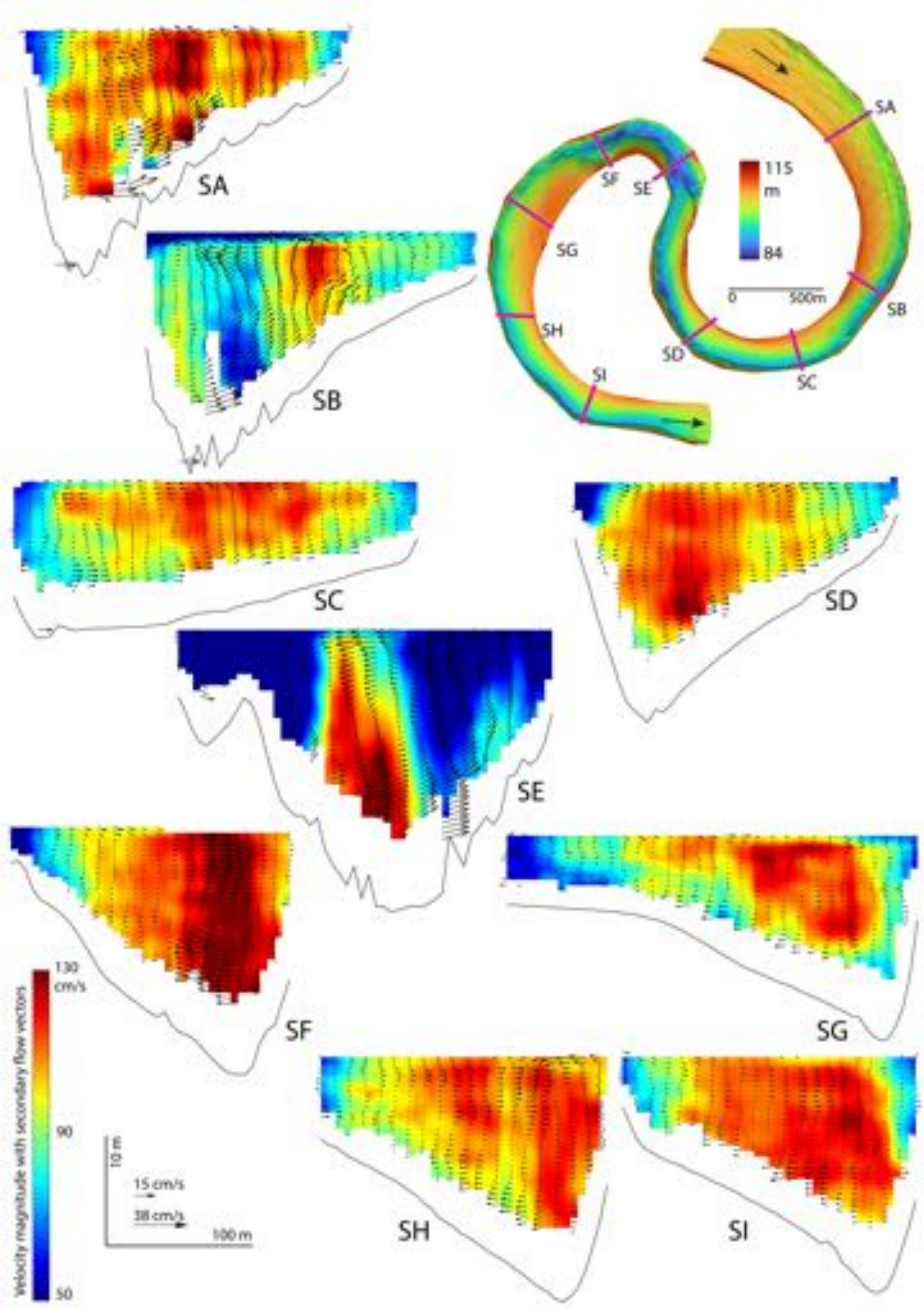

Figure 16. May 2021: ADCP measurements along the DS-skwed (HS) and US-skewed(HS) bends. $Q_w = 2880m^3/s$ (averaged [over the entire campaign] water discharge)

served. In general, for higher flows, higher intensity secondary flows are observed. Similar transverse bed slopes are observed for February 2020 and May 2021´s field measurements.

4 Discussion

4.1 Linking planform configuration to bed morphology and flow structure

Considering the laboratory experiments for US- and DS-skewed conditions (with constant width condition), specially in Figure 9, for the US- (DS-skewed) condition, there is a transitional region between CS13 and CS14 (CS18 to CS17), where the bed morphology adapts rapidly to the local change in curvature. For super-resonant conditions (experiments with reach-averaged water depth of 2 cm), the inner bank depositional region moves slightly upstream compared to the sub-resonant condition. Based on the field measurements along the Tigre River (Figure 10), steady bed morphology is influenced mainly by local curvature, width variations and the presence of bedforms (similar to Abad & Garcia (2009b)). As observed in Figures 14 and 16, width variations (as opposite to the experimental condition in the Kinoshita channel) cause changes in the secondary flow structure. Thus, at field scale such as in the Tigre River (where more DS-skewed bends are observed), the influence of morphodynamic regime (sub-resonant or super-resonant) might be filtered out by additional influencing factors (e.g. floodplain soil heterogeneity, presence of paleochannels, width variations) that are acting simultaneously.

4.2 Upstream and downstream influence on river migration

As observed by the normalized time-averaged bed morphology for the Kinoshita flume experiments (Figure 9) for the US-skewed case (considering a half-bend configuration, 5m long from CS13 to CS18), the outer bank erosional region is located from CS14 to CS17 (3 meters long, 60% of the half-bend), while for the DS-skewed configuration, the erosional region is located from CS17.5 to CS12.5 (5 meters long, 100% of the half-meander). Considering that lateral migration rates are correlated to erosional regions along the outer bank, the US-skewed bends might migrate to preserve their skewness, having the maximum migration near the deepest outer bank region (around CS14.5). For the DS-skewed bends, the lateral migration might be more homogeneous and along the entire bend, having the maximum migration around CS14.5, thus preserving the bend skewness. At field scale, based on Figure 1E, the DS(HS) bend migrates faster (and along the entire bend) than the US(HS) bend (similar results as the flume experiments). For the US(HS) bend, the highest migration does not occur at the maximum curvature location (near S14), since there is a slight width variation and an effect from the DS(HS) located upstream of the bend. In high-sinuosity and high-amplitude conditions, and in different morphodynamic regimes, bends try to preserve their skewness, therefore the question on why bends change skewness (as correlated to sinuosity or other metrics) still remains unanswered. As observed in Figure 1, the Tigre River presents paleochannels (of different sinuosities and orientations) along the river valley, producing a heterogeneous distribution of sediments throughout the floodplain, thus, when the modern planform configuration of the Tigre River interacts with these paleochannels, local adjustments and planform reconfiguration might occur. More detailed studies are needed to understand how the main channel reconnects to paleochannels and oxbow lakes, and how important re-connectivity is to develop certain type of bend orientation.

4.3 Nonlinear effects on morphodynamic regimes

Indeed, Colombini et al. (1992) described how linear models cannot describe the interactions of migrating bars over fixed bars (Kinoshita & Miwa (1974),Whiting & Dietrich (1993b,c,a)), besides linear models cannot account for flow separation and in general the complex flow structures at high-curvature and high-amplitude bends. It is also known that interactions between free and forced patterns are responsible for some nonlinear effects that control bed topography in meanders (Seminara, 1989). The experimental design used in this study was based on the concept of morphodynamic regimes (sub- and super-resonant) that is derived from linear approximation, and in high-curvature and high-amplitude meandering configurations, nonlinear effects are important, thus, phase diagrams for natural rivers should be developed by using fully nonlinear depth-averaged models such as in Abad et al. (2008), Langendoen et al. (2016) and Codier et al. (2019). It is important to consider width variations in field scale analysis; in the Tigre River, even though there is a small width oscillation, bed morphology and more importantly flow structure are significantly affected.

5 Conclusions

Based on the experiments in the Kinoshita flume, DS-skewed bends produce more developed bedforms (higher bedform roughness) than US-skewed bends (for all sub- and super-resonant conditions); however, planform roughness are larger for US- than DS-skewed bends;this explains why water surface streamwise slopes for DS-skewed conditions are slightly lower than those for US-skewed conditions. Based on the laboratory experiments with constant channel width, inner bank depositional regions for super-resonant conditions migrate slightly upstream compared with the sub-resonant conditions; this was not verified at natural scale because the Tigre River is characterized by sub-resonant condition. Based on the field analysis of the Tigre River, bedforms dominate roughness especially along low sinuosity reaches, because bedforms are reduced in size along bends due to curvature effects. Perturbations in channel width and local curvature modify locally the morphology and flow structure (primary and secondary flow) at field scale, thus, affecting sediment transport and bed morphology of the river. Development of fully nonlinear morphodynamic models for the prediction of bed morphology and flow structure in super-resonant and sub-resonant regimes is needed to account for field nonlinearities. Field scale conditions filter out the influence of morphodynamic regimes in high-sinuosity meandering channels, where bends tend to preserve their skewness if no external forcing is considered.

Acknowledgments

Thanks to Gary Parker and the Department of Civil and Environmental Engineering of the University of Illinois at Urbana-Champaign for providing financial support for the construction of the Kinoshita flume. Thanks also for the support received through several grants (PI Garcia): STAR program of the U.S. Environmental Protection Agency (EPA), Illinois Water Resources Center (IWRC), and the Metropolitan Water Reclamation District of Greater Chicago (MWRDGC). The field measurements were supported by the Gordon and Betty Moore Foundation under Grant Agreement 7711 (PI Abad) and collaboration with the National Service of Meteorology and Hydrology-SENAMHI-Loreto. The authors thank the research field assistants Flor Fuentes, Bryan Santillan, Yulissa Estrada at UTEC and Jhonatan Perez, and Hernan Gonzales at SENAMHI-Loreto. Thanks to RED YAKU´s assistant Wendy Roque and Tania Rojas for helping with GIS maps and proofreading the manuscript.

References

Abad, J. D. (2005). Cfd simulations of asymmetric kinoshita-generated meandering bends. *XXXI International Association of Hydraulic Engineering and Research (IAHR) Congress, September 11-16, Seoul, Korea*, 10 pp.

Abad, J. D., Buscaglia, G. C., & Garcia, M. H. (2008). 2d stream hydrodynamic, sediment transport and bed morphology for engineering applications. *Hydrological Processes*, *22*, 1443-1459. doi: 10.1002/hyp.6697

Abad, J. D., Frias, C. E., Buscaglia, G. C., & Garcia, M. H. (2013). Modulation of the flow structure by progressive bedforms in the kinoshita meandering channel. *Earth Surface Processes and Landforms*, *38*(13), 1612-1622.

Abad, J. D., & Garcia, M. H. (2009a). Experiments in a high-amplitude kinoshita meandering channel. 1: Implications of bend orientation on mean and turbulent flow structure. *Water Resources Research*, *45*. doi: 10.1029/2008WR007016

Abad, J. D., & Garcia, M. H. (2009b). Experiments in a high-amplitude kinoshita meandering channel. 2: Implications of bend orientation on bed morphodynamics. *Water Resources Research*. doi: 10.1029/2008WR007016

Abad, J. D., Mendoza, A., Arceo, K., Torres, Z., Valverde, H., Medina, G., . . . Berezowsky, M. (2022). Planform dynamics and cut-off processes in the lower ucayali river, peruvian amazon. *Water*, *14*(3059). doi: https://doi.org/10.3390/w14193059

Abad, J. D., Sequeiros, O. E., Pirmez, C., Garcia, M. H., & Parker, G. (2011). Secondary current of saline underflow in a highly meandering channel: Experiments and theory. *Journal of Sedimentary Research*, *81*(11), 787-813.

Almeida, R. P., Freitas, B. T., Turra, B. B., Figueiredo, F. T., Marconato, A., & Janikian, L. (2016). Reconstructing fluvial bar surfaces from compound cross-strata and the interpretation of bar accretion direction in large river deposits. *Sedimentology*, *63*(3), 609–628.

Bernal, C., Christohoul, F., Darrozes, J., Soula, J.-C., Baby, P., & Burgos, J. (2011). Late glacial and holocene avulsions of the rio pastaza megafan (ecuador- peru): frequency and controlling factors. *International Journal of Earth Siences*, *100*, 1759-1782.

Bertagni, M. B., & Camporeale, C. (2018). Finite amplitude of free alternate bars with suspended load. *Water Resources Research*, *54*, 9759-9773.

Blondeaux, P., & Seminara, G. (1985). A unified bar-theory of river meanders. *Journal of Fluid Mechanics*, *157*, 449-470.

CITA. (2019). Metodología de línea base geomorfológica para los ríos de la hidrovía amazónica, aplicación en el río huallaga. , 12. Retrieved from `https://www.dancingrivers.com/publicaciones`

CITA. (2021). Ríos danzantes, guías metodológicas para el desarrollo de la línea base física de los ríos en andes-amazonía. , 346. Retrieved from `https://www.dancingrivers.com/publicaciones`

Codier, F., Tassi, P., Claude, N., Crosato, A., Rodrigues, S., & Bang, D. V. (2019). Numerical study of alternate bars in alluvial channels with nonuniform sediment. *Water Resources Research*, *55*, 2976-3003.

Colombini, M., Seminara, G., & Tubino, M. (1987). Finite-amplitude alternate bars. *Journal of Fluid Mechanics*, *181*.

Colombini, M., Tubino, M., & Whiting, P. (1992). Topographic expression of bars in meandering channels. *In Dynamics of Gravel-bed rivers. Edited by P. Billi, R. D. Hey, C. R. Thorne and P. Tacconi. John Wiley and Sons Ltd.*.

Dinehart, R., & Burau, J. R. (2005). Averaged indicators of secondary flow in repeated acoustic doppler current profiler crossing of bends. *Water Resources Research*, *41*, 1-18.

Garcia, M. H., & Nino, Y. (1993). Dynamics of sediment bars in straight and meandering channels: experiments on the resonance phenomenon. *Journal of Hydraulic Research*, *31*(6), 739-761.

Guerrero, L., Abad, J., Ortals, C., Naito, K., Valverde, H., Estrada, Y., … Canas, C. (2022). The birthplace of the amazon river, a confluence of anabranching and meandering rivers. *Under review in Water Resources Research*.

Guneralp, I., & Marston, R. (2012). Process-form linkages in meander morphodynamics. *Progress in Physical Geography*, 1-29.

Guo, X., Chen, D., & Parker, G. (2019). Flow directionality of pristine meandering rivers is embedded in the skewing of high-amplitude bends and neck cutoffs. *Proceedings of the National Academy of Sciences*, *116*(47), 23448-23454.

Gutierrez, R., Abad, J., Parsons, D., & Best, J. (2013). Discrimination of bedforms scales using robust spline and wavelet transforms: methods and application to synthetic signals and the parana river, argentina. *Journal of Geophysical*

Research-Earth-Surface, *118*, 1400-1419.

Gutierrez, R., Mallma, J., Nunez-Gonzalez, F., Link, O., & Abad, J. (2018). Bedforms-atm, an open source software to analyze the scale-based hierarchies and dimensionality of natural bed forms. *SoftwareX*, *7*, 184-189.

Hall, P. (2004). Alternating bar instabilities in unsteady channel flows over erodible beds. *Journal of Fluid Mechanics*, *499*, 49-73.

Hickin, E. J. (1974). Development of meanders in natural river-channels. *American Journal of Science*, *274*(4), 414-442.

Ielpi, A., Ghinassi, M., Rainbird, R. H., & Ventra, D. (2018). Planform sinuosity of proterozoic rivers. In *Fluvial meanders and their sedimentary products in the rock record* (p. 81-118). John Wiley and Sons, Ltd. Retrieved from `https://onlinelibrary.wiley.com/doi/abs/10.1002/9781119424437.ch4` doi: https://doi.org/10.1002/9781119424437.ch4

Ielpi, A., M.G.A.Lapotre, Finotello, A., & Ghinassi, M. (2021). Planform-asymmetry and backwater effects on river-cutoff kinematics and clustering. *Earth Surface Processes and Landforms*, *46*(2), 357-370.

Ikeda, S., Parker, G., & Sawai, K. (1981). Bend theory of river meanders. part 1. linear development. *Journal of Fluid Mechanics*, *112*, 363-377.

Jackson, R. (1976). Depositional model of point bars in the lower wabash river. *Journal of Sedimentary Petrology*(3), 579-594.

Kinoshita, R. (1961). Investigation of channel deformation in ishikari river. *Report of the Bureau of Resources*, 1-174.

Kinoshita, R., & Miwa, H. (1974). River channel formation which prevents downstream translation of transverse bars. *ShinSabo*(94), 12-17.

Konsoer, K., B.Rhoads, J.L.Best, Langendoen, E., J.D.Abad, D.R.Parsons, & M.H.Garcia. (2016). Three-dimensional flow structure and bed morphology in large elongate meander loops with different outer bank roughness characteristics. *Water Resources Research*, *52*(12), 9621-9641.

Langendoen, E. (2000). Concepts-conservational channel evolution and pollutant transport system. *Research Report No. 16, USDA-ARS National Sedimentation Laboratory, Oxford, MS. USA*.

Langendoen, E., A.Mendoza, J.D.Abad, P.Tassi, D.Wang, R.Ata, ... Hervouet, J.-M. (2016). Improved numerical modeling of morphodynamics of rivers with steep banks. *Advances in Water Resources*, *93*(A), 4-14.

Lanzoni, S., & Seminara, G. (2006). On the nature of meander instability. *Journal of Geophysical Research: Earth Surface*, *111*(F4).

Latrubesse, E., J.C.Stevaux, & Sinha, R. (2005). Tropical rivers. *Geomorphology*, *70*, 187-206.

Leopold, L. B., & Langbein, W. B. (1966). River meanders. *Scientific American*, *214*, 60-70.

Monegaglia, F., M.Tubino, & G.Zolezzi. (2019). Interactions between curvature-driven width oscillations and channel curvature in evolving meander bends. *Journal of Fluid Mechanics*, *876*(7), 985-1017.

Motta, D., Abad, J. D., Langendoen, E. J., & García, M. H. (2012). The effects of floodplain soil heterogeneity on meander planform shape. *Water Resources Research*, *48*(9). Retrieved from `https://agupubs.onlinelibrary.wiley.com/doi/abs/10.1029/2011WR011601` doi: https://doi.org/10.1029/2011WR011601

Motta, D., Langendoen, E. J., Abad, J. D., & García, M. H. (2014). Modification of meander migration by bank failures. *Journal of Geophysical Research: Earth Surface*, *119*(5), 1026-1042. Retrieved from `https://agupubs.onlinelibrary.wiley.com/doi/abs/10.1002/2013JF002952` doi: https://doi.org/10.1002/2013JF002952

Mueller, D. S., & Wagner, C. R. (2007). Correcting acoustic doppler current profiler discharge measurements biased by sediment transport. *Journal of Hydraulic Engineering*, *133*(12), 1329–1336.

Oberg, K., & Mueller, D. S. (2007). Validation of streamflow measurements made with acoustic doppler current profilers. *Journal of Hydraulic Engineering*, *133*(12), 1421–1432.

Parker, G. (1976). On the cause and characteristics scales of meandering and braiding in rivers. *Journal of Fluid Mechanics*(76), 457-480.

Parker, G., & Andrews, E. (1986). On the time development of meander bends. *Journal of Fluid Mechanics*, *162*(9), 139-156.

Parker, G., Diplas, P., & Akiyama, J. (1983). Meander bends of high amplitude. *Journal of Hydraulic Engineering*, *109*(10), 1323-1337.

Parsons, D. R., Best, J. L., Orfeo, O., Hardy, R. J., Kostaschuk, R., & Lane, S. N. (2005). Morphology and flow fields of three-dimensional dunes, rio paraná, argentina: Results from simultaneous multibeam echo sounding and acoustic doppler current profiling. *Journal of Geophysical Research: Earth Surface*, *110*(F4). Retrieved from `https://agupubs.onlinelibrary.wiley.com/doi/abs/10.1029/2004JF000231` doi: https://doi.org/10.1029/2004JF000231

Parsons, D. R., Jackson, P., Czuba, J. A., Engel, F., Rhoads, B. L., Oberg, K., ... Riley, J. (2013). Velocity mapping toolbox (vmt): a processing and visualization suite for moving-vessel adcp measurements. *Earth Surface Processes and Landforms*, *38*(11), 1244–1260.

Ruben-Dominguez, L., Naito, K., Gutierrez, R., R.Szupiany, & Abad, J. D. (2021). Meander statistics toolbox (mstat): a toolbox for geometry characterization of bends in large meandering channels. *SoftwareX*, *14*.

Seminara, G. (1989). Meander migration prediction by a. crosato - linear and non linear theory meanders by m. tubino. *Excerpta*, *4*.

Seminara, G. (2010). Fluvial sedimentary patterns. *Annual Review of Fluid Mechanics*, *42*, 43-66.

Seminara, G., & Tubino, M. (1992). Weakly nonlinear theory of regular meanders. *Journal of Fluid Mechanics*, *244*, 257-288.

Seminara, G., Zolezzi, G., Tubino, M., & Zardi, D. (2001). Downstream and upstream influence in river meandering. part 2. planimetric development. *Journal of Fluid Mechanics*, *438*.

Shan, J., Z.P.Lin, Chen, L., Zhang, B., Fang, S., Yan, X., ... Zhang, L. (2018). Reconstruction of meandering paleo-channels using dense well data, daqing oil field, songliao basin, china. *Petroleum Science*, *15*, 722-743.

Slowik, M. (2015). The inflience of meander bend evolution on the formation of multiple cutoffs: findings inferred from floodplain architecture and bend geometry. *Earth Surface Processes and Landforms*, *41*(5), 626-641.

Tubino, M., & Seminara, G. (1992). Free-forced interactions in developing meanders and suppression of free bars. *Journal of Fluid Mechanics*, *214*, 131-159.

Whiting, P. J., & Dietrich, W. E. (1993a). Experimental constrains on bar migration through bends: Implications for meander wavelength selection. *Water Resources Research*, *29*(4), 1091-1102.

Whiting, P. J., & Dietrich, W. E. (1993b). Experimental studies of bed topography and flow patterns in large-amplitude meanders 1. observations. *Water Resources*

Research, *29*(11), 3605-3614.

Whiting, P. J., & Dietrich, W. E. (1993c). Experimental studies of bed topography and flow patterns in large-amplitude meanders 2. mechanisms. *Water Resources Research*, *29*(11), 3615-3622.

Zolezzi, G., Guala, M., Termini, D., & Seminara, G. (2005). Experimental observations for upstream overdeepening. *Journal of Fluid Mechanics*, *531*, 191-219.

Zolezzi, G., & Seminara, G. (2001). Dowstream and upstream influence in river meandering. part 1. general theory and application to overdeepening. *Journal of Fluid Mechanics*, *438*, 183-211.

Supplemental Material - Hydrogeomorphology of asymmetric meandering channels: experiments and field evidence

J. D. Abad[1,2], D. Motta[3], L. Guerrero[4,5], M. Paredes[6], J. M. Kuroiwa[1], and M.H. Garcia[7]

[1]Universidad Nacional de Ingenieria, Lima, Peru
[2]RED YAKU, Lima, Peru
[3]Northumbria University, Newcastle upon Tyne, UK
[4]Lousiana State University, USA
[5]Universidad de Ingenieria y Tecnologia, Lima, Peru
[6]National Service of Meteorology and Hydrology-SENAMHI, Loreto, Peru
[7]University of Illinois at Urbana-Champaign, Illinois, USA

1 Critical and resonant morphodynamic conditions

Applying the linear instability theory to the 2D depth-averaged Saint Venant equations, Blondeaux & Seminara (1985), Colombini et al. (1987), Tubino et al. (1999) and Seminara (2010) developed an algebraic dispersion relationship (Equation 1) where the growth rate (Ω, real part) and angular frequency (ω, imaginary part) are given by Equations (2) and (3), respectively.

$$\frac{(\Omega - m\omega i)}{Q_0\Phi_0} = -\frac{A_0 + iA_1\lambda + A_2\lambda^2 + iA_3\lambda^3 + A_4\lambda^4}{B_0 + iB_1\lambda + B_2\lambda^2 + iB_3\lambda^3} \tag{1}$$

$$\Omega = -Q_0\Phi_0 \frac{[(A_0 + A_2\lambda^2 + A_4\lambda^4)(B_0 + B_2\lambda^2) + (A_1\lambda + A_3\lambda^3)(B_1\lambda + B_3\lambda^3)]}{(B_0 + B_2\lambda^2)^2 + (B_1\lambda + B_3\lambda^3)^2} \tag{2}$$

$$\omega = \frac{Q_0\Phi_0}{m} \frac{[(B_0 + B_2\lambda^2)(A_1\lambda + A_3\lambda^3) - (A_0 + A_2\lambda^2 + A_4\lambda^4)(B_1\lambda + B_3\lambda^3)]}{(B_0 + B_2\lambda^2)^2 + (+B_1\lambda + B_3\lambda^3)^2} \tag{3}$$

where: $A_0 = -(\frac{\pi^2}{4})^2 m^3 C_0 R s_1 \beta$, $A_1 = \frac{\pi^2}{4}[(F_0^2 C_0^2 R\beta + C_0)(s_2 - s_1 - 1)m\beta - m^2 C_0 \beta(f_1(s_2 - 1) - f_2 s_1) - m^4 R\frac{\pi^2}{4}]$, $A_2 = m^3\frac{\pi^2}{4}(1 - f_2 - C_0 R\beta - F_0^2 C_0 R\beta(s_2 - s_1 - 2))$, $A_3 = (F_0^2 - 1)m^4 R\frac{\pi^2}{4} - C_0(f_1 - f_2)m^2\beta$, $A_4 = (f_1 - f_2)m^3$, $B_0 = -\frac{\pi^2}{4}s_1 C_0 \beta m$, $B_1 = F_0^2\beta^2 C_0^2(s_2 - s_1 - 1) - m^2\frac{\pi^2}{4}$, $B_2 = (F_0^2(s_1 - s_2 + 2) - 1)mC_0\beta$, $B_3 = (F_0^2 - 1)m^2$

λ is the dimensionless real longitudinal wave number scaled by the channel half-width (B^*). m is the Fourier lateral mode (where $m = 1$ is the one related to alternate bars). Q_0 is the scale of sediment discharge to the flow rate ($= \frac{d_s^*\sqrt{Rgd_s^*}}{(1-p)D_0^* U_0^*}$), p is the porosity. $\beta = \frac{B^*}{H_0^*}$ is the half width-to-depth ratio. $d_s = \frac{d_s^*}{H_0^*}$ is the dimensionless sediment size (d_s^* is the sediment size with dimensions). $R = \rho_s/\rho - 1$, where ρ_s and ρ are the sediment and water density. U_0^*, H_0^*, C_0, $F_0 = \frac{U_0^*}{\sqrt{gH_0^*}}$ are the unperturbed (uniform flow) longitudinal velocity, water depth, friction coefficient, and Froude number, respectively. Fore more details on the variables (s_1, s_2, f_1, f_2) and the linear stability analysis, please read Blondeaux & Seminara (1985) and Colombini et al. (1987). Figure 1a shows the stability diagram where one can observe the stable and unstable conditions, the direction where the perturbation would travel to, and the critical and resonant conditions.

Corresponding author: Jorge D. Abad, jabad@redyaku.com

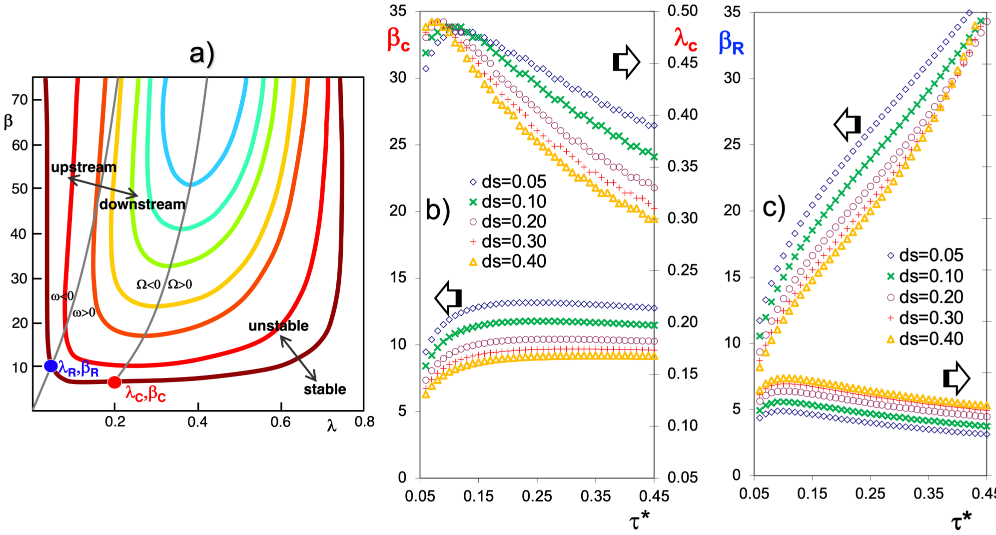

Figure 1. a) Stability diagram based on linear modeling. b) Critical (β_C,λ_C) and c) resonant (β_R,λ_R) conditions for different Shields stress (τ^*) and dimensionless sediment sizes (d_s). For the analysis, Parker (1990)´s bedload predictor was used.

Figures 1b and 1c show β_C and λ_C (critical values) and β_R and λ_R (resonance values) for different values of Shields stress and nondimensional sediment size.

2 Experimental selection of the sediment size

In a recirculating flume (for water and sediment) with fixed channel width (60 cm), the sediment bed slope is an outcome from the experiments (after recirculating for more than 200 hours as described by Abad & Garcia (2009)), thus, phase diagrams for the linear stability analysis to predict the sub- and super-resonant conditions were developed for slopes ranging from 0.001 to 0.010. Herein, Parker (1990)´s sediment transport equation is employed as follows

$$q^* = 0.00218(\tau^{*3/2})G(\xi) \tag{4}$$

where $G(\xi) = 5474(1 - \frac{0.853}{\xi})^{4.5}$ if $\xi \geq 1.59$, $G(\xi) = exp[14.2(\xi - 1) - 9.28(\xi - 1)^2]$ if $1.0 \leq \xi \leq 1.59$, and $G(\xi) = \xi^{14.2}$ if $\xi \leq 1$, $\xi = \frac{\tau^*}{0.0386}$, and q^* is the sediment transport rate.

Figure 2 shows plots of τ^* vs S_s (longitudinal water surface slope) for particle sediment sizes of D^*_{s50} =0.543 mm, 0.832 mm, and 1.331 mm where threshold equations for motion, suspension and for the presence of ripples are described by $\tau^*_{motion} = 0.5[0.22Re_p^{-0.6} + 0.0610^{-7.7Re_p^{-0.6}}]$, $\tau^*_{suspension} = \frac{u_*^2}{gRD^*_{s50}}$, and $\tau^*_{ripples} = (\frac{11.6}{Re_p})^2$, respectively ($R_p = \frac{V_s D^*_{s50}}{\nu}$, $Re_p = \frac{\sqrt{RgD^*_{s50}}D^*_{s50}}{\nu}$, $C_D = \frac{24}{R_p}(1 + 0.152R_p^{1/2} + 0.015R_p)$, $V_s = \sqrt{\frac{4}{3}gR\frac{D^*_{s50}}{C_D}}$, ν is the kinematic viscosity). The idea behind these diagrams is to support the design of experimental conditions for sub- and super-resonant conditions. For all three diagrams, when $H^* = 1cm$ ($\beta = 30$), the regime is super-resonant ($\tau^* < \tau_R$) regime and allows bars ($\tau^* < \tau_C$). For $H^* = 2cm$ ($\beta = 15$), for $D^*_{s50} = 0.832mm$ and $D^*_{s50} = 0.1331mm$, the condition is super-resonant regime with presence of bars for all slopes, however for $D^*_{s50} = 0.543mm$, for $S_s > 0.006$, the regime is sub-resonant with presence of bars. For $H^* = 3cm$ ($\beta = 10$), for $D^*_{s50} = 0.543mm$ and $S_s > 0.004$, the regime is sub-resonant without the presence of bars, and for $D^*_{s50} = 0.832mm$ ($S_s > 0.003$) and $D^*_{s50} = 1.331mm$

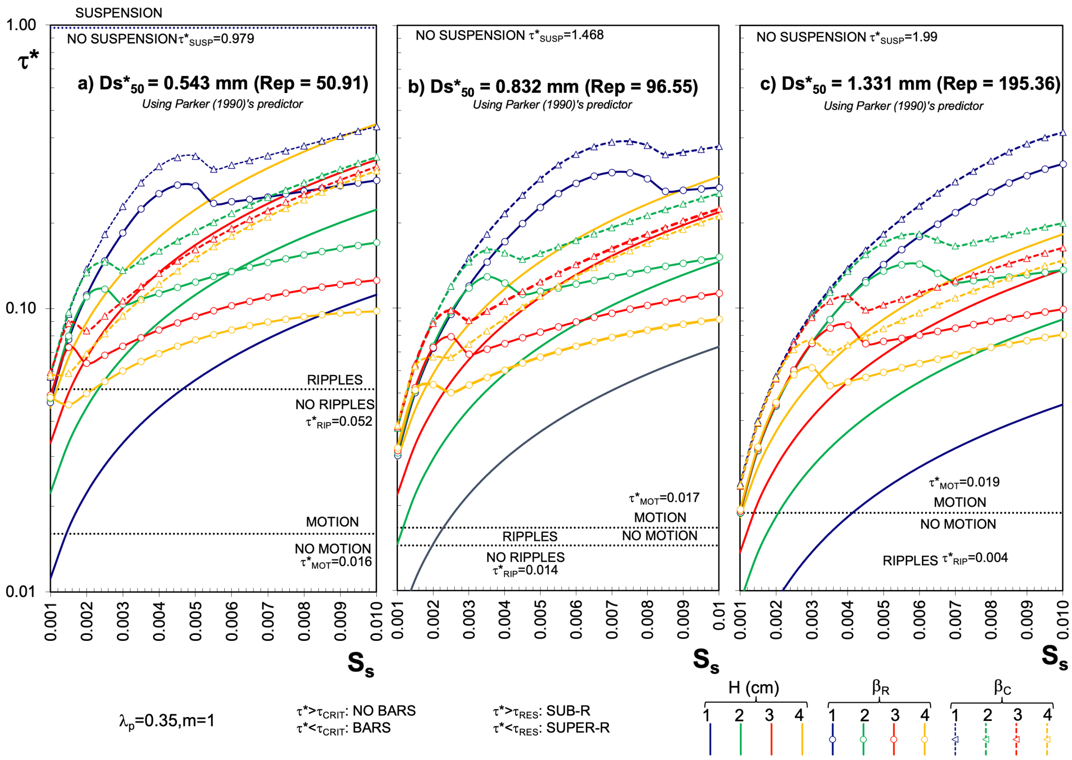

Figure 2. Sensitivity analysis for the design of experiments. Phase diagrams for different sediment particle size (D^*_{s50}).

($S_s > 0.006$), the regime is sub-resonant with presence of bars. For $H^* = 4cm$ ($\beta = 7.5$), and for the majority of slopes S_s, the regime is sub-resonant without the presence of bars. Based on this analysis and in order to have suitable experimental conditions for both sub- and super-resonant conditions, $D^*_{s50} = 0.832mm$ was selected. A similar analysis using a different bedload sediment transport predictor (Wong & Parker, 2006) was performed, the results were analogous to those obtained with Parker (1990)´s predictor.

References

Abad, J. D., & Garcia, M. H. (2009). Experiments in a high-amplitude kinoshita meandering channel. 2: Implications of bend orientation on bed morphodynamics. *Water Resources Research*. doi: 10.1029/2008WR007016

Blondeaux, P., & Seminara, G. (1985). A unified bar-theory of river meanders. *Journal of Fluid Mechanics*, *157*, 449-470.

Colombini, M., Seminara, G., & Tubino, M. (1987). Finite-amplitude alternate bars. *Journal of Fluid Mechanics*, *181*.

Parker, G. (1990). Surface-based bedload transport relation for gravel rivers. *Journal of Hydraulic Research*, *28*(4), 417-436.

Seminara, G. (2010). Fluvial sedimentary patterns. *Annual Review of Fluid Mechanics*, *42*, 43-66.

Tubino, M., Repetto, R., & Zolezzi, G. (1999). Free bars in rivers. *Journal of Hydraulic Research*, *37*(6), 759-775.

Wong, M., & Parker, G. (2006). Reanalysis and correction of bed-load relation of meyer-peter and muller using their own database. *Journal of Hydraulic Engineer-*

ing, *132*(11).